ENERGY LANDSCAPE STATISTICS AND COARSENING IN LIQUIDS: A RELAXATION MODE ANALYSIS

BY

ZHIKUN CAI

THESIS

Submitted in partial fulfillment of the requirements
for the degree of Master of Science in Nuclear, Plasma, and Radiological Engineering
in the Graduate College of the
University of Illinois at Urbana-Champaign, 2016

Urbana, Illinois

Master's Committee:

Assistant Professor Yang Zhang, Adviser
Professor Rizwan Uddin

Abstract

Energy landscape, the high dimensional energy surface in the configuration space, has been widely applied to interpret slow processes that occur over a long time scale, such as slow relaxations of supercooled liquids approaching the glass transition. Despite extensive simulation studies, experimental characterization of the energy landscape still remains a challenge. To address this challenge, in this work, we developed a relaxation mode analysis (RMA) for liquids under a framework analogous to the normal mode analysis for solids. Using RMA, complicated relaxations of liquids are decoupled into a distribution of relaxation modes, from which important statistics of relaxation times and activation barriers on the energy landscape become accessible from experimentally measurable two-point density-density correlation functions, e.g. using quasi-elastic and inelastic scattering experiments. As demonstrations, this RMA approach was used to analyze three empirical models, i.e. exponential relaxation, stretched exponential relaxation, and relaxation arising from normally distributed activation energies. Furthermore, we applied RMA to study the relaxations of a Kob-Andersen liquid when dynamical cooperativity emerges in the landscape-influenced regime using molecular dynamics simulations. The results revealed a prominent dynamic decoupling and a coarsening effect of the energy landscape at different length scales. These demonstrations suggest that RMA is a promising tool to extract energy landscape statistics from experimental data. In the end, we discuss the future extensions of RMA from both application and theoretical perspectives.

Acknowledgments

First of all, I would like to express my sincere gratitude to my supervisor, Professor Yang Zhang. This work would not have been possible without his strong support. Besides, I learned more than scientific knowledge from him in the course of working on this project. His dedication to scientific research teaches me a lot about what a professional scientist is like.

Besides, I really appreciate the time and efforts that Professor Rizwan Uddin and Professor James Stubbins invested to help me improve this thesis. Also, I want to thank my labmates, Abhishek Jaiswal, Ke Yang, and Nathan Walter for their instructive discussions. Thanks to their kind help during the past two years, studying and living abroad for the first time became much easier for me.

Finally, I want to thank my family for their love and support throughout my life.

Table of Contents

List of Tables

List of Figures

List of Abbreviations

MD	Molecular Dynamics
RMA	Relaxation Mode Analysis
RR-PDF	Relaxation Rate Probability Density Function
RT-PDF	Relaxation Time Probability Density Function
AE-PDF	Activation Energy Probability Density Function
A-R	Activation-Relaxation
ILT	Inverse Laplace Transform
LASSO	Least Absolute Shrinkage and Selection Operator
RNNLS	Regularized Non-Negative Least Squres
LDP	Least Distance Programming
MSD	Mean Square Displacement

Chapter 1

Introduction

1.1 Supercooled Liquids and Glasses

Glassy materials are ubiquitous in daily life and technological applications [1, 2]. Window glasses made from sand (mainly silica) are the most common engineering amorphous solids [3]. Most communication networks rely on large amount of optical fibers made from amorphous silica. Metallic glasses made of multiple metallic elements exhibit promising properties such as soft magnetism, high strength, and remarkable resistance to corrosion [4, 5]. Besides inorganic glasses, organic glasses have been used in the design of organic electronics [6, 7]. Food and biomedical samples can be preserved by utilizing their glassy states [8, 9]. Such broad applications of glasses has attracted a lot of research attentions.

Besides a wide range of applications, glasses and their formation yield fundamental challenges in the course towards understanding randomness and cooperativity. Unlike crystalline solids, glasses are disordered materials lacking long-range structural periodicity. They are typically prepared by quenching liquids fast enough such that crystallization is avoided. Figure 1.1 illustrates the temperature dependence of volume (v) and enthalpy (h) towards the formation of glasses [1, 3]. Upon cooling, liquids become supercooled and increasingly viscous below the melting temperature T_m . Abrupt but continuous changes in the thermal expansion coefficient $\alpha_p = (\partial \ln v/\partial T)_p$ and the isobaric heat capacity $\alpha_p = (\partial h/\partial T)_p$ signify the glass transition occurring at T_g. The higher the cool rate, the lower the glass transition temperature T_g. Despite subtle structural change from liquids to glasses, vast increase of characteristic relaxation time over many orders of magnitude was observed. This apparent inconsistency between structural and dynamical changes has been of longstanding research interest. For this reason, glasses are often conceptually considered as liquids that are arrested in certain configurations and structural relaxation occurs over a much longer timescale than that in laboratory observation.

Supercooled liquids exhibit very different dynamical behaviors compared to liquids at high temperatures. One of the most striking differences is the emergence of dynamic heterogeneity at low temperatures. Dynamic heterogeneity refers to the existence of spatially dynamic fluctuations when a liquid system approaches its

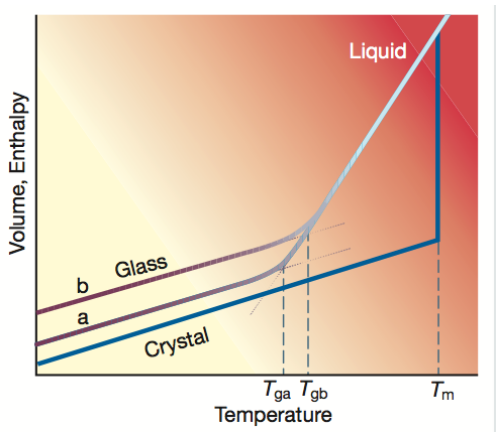

Figure 1.1: Illustration of the glass transition upon supercooling. A liquid becomes supercooled below its melting temperature T_m if crystallization is somehow avoided, for example, by fast quenching. The supercooled liquid undergoes the glass transition at T_g. The transition path "b" has a higher cooling rate than the path "a". The higher the cool rate, the lower T_g. (Adapted from Fig. 1 in Ref. [1])

glassy state [10, 11, 12, 13]. At high temperatures, particles move independently and the system exhibits homogeneous dynamics characterized by a well defined relaxation time. As temperature decreases and dynamics becomes increasingly sluggish, particles experience severer local confinements by cages formed by nearest neighbors. Under such circumstance, cooperativity starts to play an important role in facilitating configurational rearrangements. Neighboring particles with similar mobilities form local clusters and migrate in cooperative manners. This physical picture is shown by Figure 1.1 [10]. Under supercooling, particles exhibit various mobilities at different spatial regions and those with similar mobilities are spatially correlated. The length scale of this spatiotemporal correlation grows substantially near the glass transtion[12, 14], as indicated by the peak growth of the non-Gaussian parameter $\alpha_2(t)$ [15] and four-point correlation function $\chi_4(t)$ [14, 16].

Such spatially heterogeneous dynamics is believed to be the underlying origin that leads to nonexponential relaxations of time correlation functions near T_g [12]. An empirical expression is given by the stretched exponential function

$$F(t) = \exp\left[-\left(\frac{t}{\tau}\right)^{\beta}\right], \tag{1.1}$$

where τ is a characteristic relaxation time and β is a stretching exponent between 0 and 1. $F(t)$ represents certain time correlation function that measures structural relaxation, such as the intermediate scattering function (see section. 1.3). Using the picture of dynamic heterogeneity, this nonexponential relaxation can be explained qualitatively. Each relaxing domain in the system follows exponential relaxation with an specific relaxation rate (time). The relaxation rate varies from one local region to another, forming a spatial distribution. Cumulative contributions from multiple relaxing domains yield nonexponential relaxation.

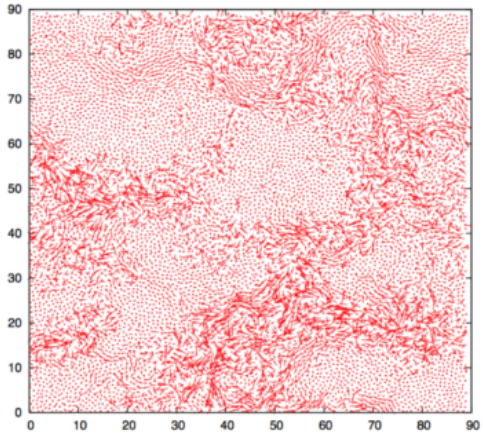

Figure 1.2: Illustration of dynamic heterogeneity: a spatial map of single particle displacements of a simulated two-dimensional Lennard-Jones mixture in a duration comparable to the structural relaxation time. (Adapted from Figure 3 in Ref. [10])

To quantify unusual properties of supercooled liquids and glass transition, various theoretical approaches have been proposed, including Adam-Gibbs theory [17], mode-coupling theory (MCT) [18, 19, 20, 21], random first order transition (RFOT) theory [22, 23, 24, 25, 26], dynamic facilitation [27]. In addition, a framework proposed by Goldstein [28] provides an intuitive picture to describe slow dynamics qualitatively. This framework is now known as energy landscape, which is our focus in next section. On the other hand, from an experimental perspective, neutron scatteringhas been proved a very useful technique in characterizing amorphous materials because of its direct accessibility to time correlation functions at appropriate length scales and time scales comparable to atomistic motions. Thus in section 1.3, we introduce the time correlation functions measurable from neutron scattering experiments. This section lays the basic languages used in the rest of this thesis and we show that the RMA approach proposed in this thesis establishes a link between the energy landscape and measurable quantities from neutron scattering experiments.

1.2 Free Energy Landscape

Many slow processes in complex systems, such as glass transition, material aging, and protein folding, still remain open topics despite intensive research efforts in the last few decades. Obstacles largely originate from the wide span of involved time scales and (or) the complexity of material constitutions. One important framework to study such slow processes is the energy landscape. Two types of energy landscapes are commonly considered, namely, the free energy landscape and potential energy landscape. The former depends on temperature, while the latter is temperature-independent. They become identical in the limit of zero temperature.

The concept of potential energy landscape was probably first introduced by Goldstein to study viscous flow [28]. Since then, this seminal idea has drawn a lot of attentions, especially in the studies of supercooled liquids towards the glass transition. For an N-body system, its potential energy landscape is a temperature-independent hyper-surface in the 3N-dimensional configuration space. Each point on the landscape evaluates the potential energy of the system corresponding to a specific configuration.

The free energy landscape extends the potential energy landscape to finite temperature, which is the focus of this thesis. Depending on the ensemble conditions, the free energy may refer to Helmholtz free energy (canonical ensemble, NVT) or Gibbs free energy (grand canonical ensemble, NPT). Unlike the potential energy landscape, the free energy landscape deforms with varying temperature. Figure 1.2 shows a schematic illustration of the energy landscape. Analogous to diverse topographical features on a geographical landscape, the energy landscape is filled with a large population of valleys (local energy minima) and hills (saddle points). Configurational mapping [29] partitions the energy landscape into a large number of basins, within which local energy minimization converges to a local energy minimum. Adjacent minima are separated by energy barriers whose heights vary from one to another. (Later in this thesis, we refer to the free energy landscape simply as the energy landscape except for those places where confusions may arise.)

The energy landscape provides an intuitive picture that facilitates the interpretations of material properties from the viewpoint of landscape topography. For example, thermodynamic properties of a liquid system are governed by the ensemble statistics of energy minima on its energy landscape. Besides the global minimum that defines the ground state, various local energy minima on the energy landscape represent metastable states. The probability for the system to occupy certain energy minimum with free energy F is weighted by the Boltzmann factor $\exp(-F/k_BT)$. The relative probability to sample two mimina with a free energy difference ΔF is given by $\exp(-\Delta F/k_BT)$. At high temperatures, overwhelming thermal energy diminishes

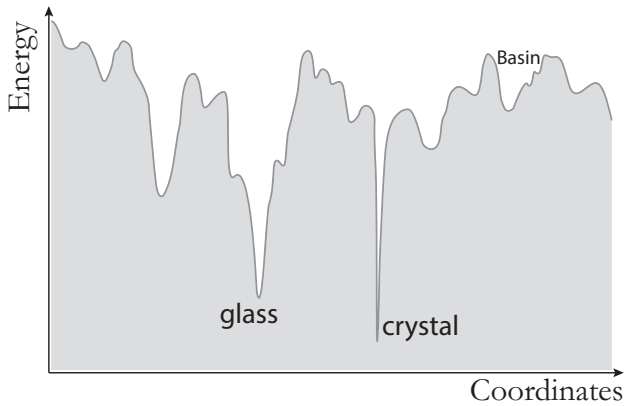

Figure 1.3: Schematic energy landscape. Conceptually, it is a multi-dimensional hyper-surface in the configuration space.

the energy difference. Accesses to different energy minima are almost equally probable. As temperature decreases, the free energy landscape deform in such a way that configurations with lower free energies become increasingly favorable at low temperatures. In addition, the dynamical behaviors of a liquid can be inferred from the manner in which the system samples its energy landscape. Configurational rearrangements as a function of time can be viewed as the motion of a state point on the energy landscape. Transitions between nearby shallow basins lead to short-time local relaxations, while transitions crossing high barriers between large basins are associated with significant atomic rearrangements and thus contribute to long-time relaxations. A system may get trapped around certain energy minimum, from which it takes tremendous waiting time to escape. Consequently, below certain crossover temperature two distinct time scales become separated, signifying the decoupling of short-time β-relaxation and long-time α-relaxation. Following this, heterogeneous dynamics emerges, leading to nonexponential relaxations. The glass transition occurs upon further cooling when the system is dynamically arrested within a local minimum.

The impact of energy landscape on the understanding of supercooled liquids and glass transition cannot be overstated. Therefore, characterizations of the energy landscape, such as the distribution of activation energy barriers, become crucial steps. So far, the knowledge base of energy landscape mainly builds upon theoretical predictions and computer simulations. Theoretical predictions are usually difficult due to the intrinsic high-dimensionality of the energy landscape. Fortunately, advanced computer powers and algorithms have been devoted to directly collect energy landscape statistics and help advance our understanding. Although many achievements have been made, computer simulations still have some limitations, e.g. regarding the capability to reflect the real physics. Hence, experimental characterization or confirmation remains a crucial component towards an integrated description of the energy landscape.

The challenge stands out that how to quantify the energy landscape statistics from experiments. In particular, the distribution of activation energy barriers on the energy landscape holds the key to interpreting liquid dynamics, which is the central interest of this thesis. In literature, only a few previous studies on metallic glasses tried to estimate the distribution of activation energy from calorimetric and shear modulus relaxation data [30, 31], as well as from stress relaxation experiments [32]. These measurements were carried out using glass samples and mainly relied on macroscopic mechanical properties. The dynamical information at microscopic scale was averaged out and remains unclear. To study microscopic dynamics, appropriate techniques measuring at timescale and length scale comparable to atomic motions are needed. One of those promising experimental techniques that have been widely used to study disordered soft matter is neutron scattering. Thus developing an approach to extract energy landscape statistics from neutron scattering data can bring up broad applications.

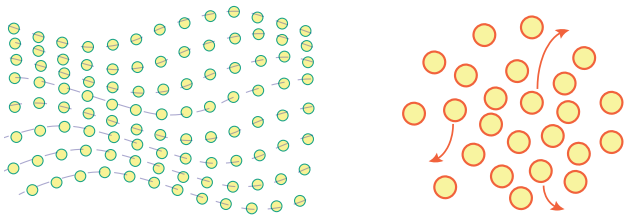

(a) Lattice vibration in solids (b) Diffusion in liquids

Figure 1.4: Schematic illustration of characteristic types of motions in solids and liquids.

To develop such an approach, a link between energy landscape properties and measurable quantities from neutron scattering needs to be established. The key quantity measured in neutron scattering experiments is the density-density correlation function, which quantifies the behavior of structural relaxations (see more details in section 1.3). From the picture of energy landscape, two extreme cases of structure relaxations can be recognized, i.e. constrained vibrations in the global minimum, and diffusions across various basins. The former exemplifies a solid, and the later represents a liquid. A careful comparison between solids and liquids provides a possibility to take advantage of more developed solid state theory.

Liquids have very different dynamics from solids (Fig. 1.4). Crystalline solids possess well defined lattices and atoms are confined to their equilibrium positions. Small atomic displacement serves as a small parameter for the theoretical development of normal mode analysis or phonon theory (for example see Ref. [33]), and lattice vibrations are considered elementary excitations. For liquids, phonons are only short-lived. Atoms can diffuse far away from their original positions. From the perspective of energy landscape, a crystal is trapped in the global minimum of its energy landscape and undergoes vibrational motions. In contrast, a liquid wanders between different basins by overcoming energy barriers and exhibit diffusive behaviors. This contrast of characteristic motions between solids and liquids makes it compelling to consider that diffusion for liquids serves as the counterpart of vibration for solids.

In this thesis, we propose an approach to extract the energy landscape statistics from the density-density correlation functions measurable from neutron scattering experiments. Under a framework analogous to the normal mode analysis for crystalline solids, we formulated a relaxation mode analysis (RMA) for liquids by assuming diffusion plays an elementary role in liquids. Using RMA, complicated relaxations of liquids can be decoupled into a distribution of relaxation rates, from which the distributions of relaxation times and activation energies can also be derived. In the following chapters, we summarize this RMA method and demonstrate its capabilities using empirical model functions and molecular dynamics simulations.

1.3 Neutron Scattering and Time Correlation Functions

Before proceeding to our approach, we would like to introduce neutron scattering, an important experimental technique in the studies of amorphous materials and soft matter, using the language of time correlation functions. These concepts form the basic languages that are used in the rest of this thesis. In this section, only some important results relevant to this thesis are summarized. For a systematic description of neutron scattering, readers can refer to an excellent book by Squires [34].

Neutron scattering is a powerful technique to probe structures and dynamics of materials at atomic scale over a timescale ranging from sub-picosecond to tens of nanoseconds. Figure 1.3 shows a typical geometry of neutron scattering. When incident neutrons are scattered by the sample, they exchange energies and momenta with the scatterers. The number of neutrons scattered into a certain solid angle is proportional to the double differential cross-section of the scatter. By measuring the distribution of scattered neutrons as a function of energy transfer and momentum transfer, physical information of the sample can be deduced. Thus neutron scattering experiments directly measure the double differential cross-section [34]

$$\frac{d^2\sigma}{d\Omega dE} = \left(\frac{d^2\sigma}{d\Omega dE}\right)_{\text{coh}} + \left(\frac{d^2\sigma}{d\Omega dE}\right)_{\text{inc}}, \tag{1.2}$$

with the coherent contribution

$$\left(\frac{d^2\sigma}{d\Omega dE}\right)_{\text{coh}} = \frac{\sigma_{\text{coh}}}{4\pi}\frac{k_f}{k_i}NS(\mathbf{k},\omega), \tag{1.3}$$

and the incoherent contribution

$$\left(\frac{d^2\sigma}{d\Omega dE}\right)_{\text{inc}} = \frac{\sigma_{\text{inc}}}{4\pi}\frac{k_f}{k_i}NS_s(\mathbf{k},\omega). \tag{1.4}$$

Here $d\Omega$ is the solid angle of scattering, E is the neutron energy, and N is the number of scatterers in

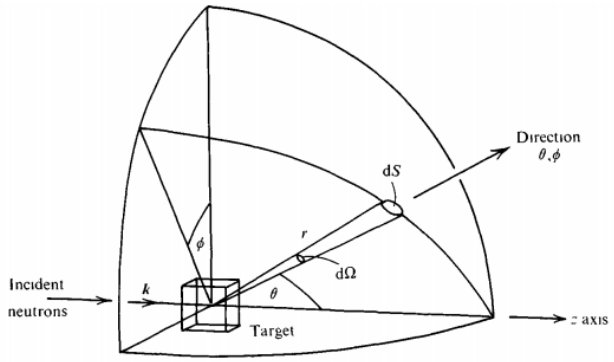

Figure 1.5: Illustration of scattering geometry. Incident neutrons along the z-axis are scattered by the targets into certain solid angle $d\Omega$ in the direction of θ, ϕ. (Adapted from Ref. [34])

the sample. k_i and k_f are the wavevectors of the incident neutron and the scattered neutron, repsectively. The momentum transfer from the neutron to the scatter is defined by $\hbar\mathbf{k} = \hbar(\mathbf{k}_i - \mathbf{k}_f)$, and the energy transfer is given by $\hbar\omega$. The main differences between the coherent and incoherent scattering lie in the material-specific microscopic cross-section σ_{coh} and σ_{inc}, as well as in the dynamic structure factor $S(\mathbf{k},\omega)$ and $S_s(\mathbf{k},\omega)$. Their physical meanings become more clear when transformed to time domain.

The coherent dynamic stucture factor $S(\mathbf{k},\omega)$ is the time Fourier transform of the coherent intermediate scattering function [34]

$$F(\mathbf{k},t) = \frac{1}{N}\sum_{j,j'}^{N}\left\langle e^{-i\mathbf{k}\cdot\mathbf{r}_j(0)}e^{i\mathbf{k}\cdot\mathbf{r}_{j'}(t)}\right\rangle = \frac{1}{N}\left\langle \rho_{\mathbf{k}}(0)\rho_{-\mathbf{k}}(t)\right\rangle, \tag{1.5}$$

where $\mathbf{r}_j(t)$ is the position of the j-th scatterer at time t, and $\langle\cdots\rangle$ stands for ensemble average. $\rho_{\mathbf{k}}(t)$ is the spatial Fourier transform of atomic density

$$\rho(\mathbf{r},t) = \sum_j \delta\{\mathbf{r} - \mathbf{r}_j(t)\}. \tag{1.6}$$

$F(\mathbf{k},t)$ quantifies the time-dependent density correlations, including the correlation between the positions of the same scatter at different times, and the correlation between the positions of different scatterers at different times. For this reason, coherent scattering measures the collective motions in materials, and $F(\mathbf{k},t)$ also represents a density-density correlation function.

In a similar manner, the incoherent dynamic structure factor $S_s(\mathbf{k},\omega)$ can be obtained by performing time Fourier transform of the incoherent intermediate scattering function [34]

$$F_s(\mathbf{k},t) = \frac{1}{N}\sum_{j}^{N}\left\langle e^{-i\mathbf{k}\cdot\mathbf{r}_j(0)}e^{i\mathbf{k}\cdot\mathbf{r}_j(t)}\right\rangle. \tag{1.7}$$

Unlike its coherent counterpart, $F_s(\mathbf{k},t)$ only depends on the correlation between the positions of the same scatterer at different times. Thus, incoherent scattering measures the self motions in materials. The relative strength of coherent and incoherent contributions depends on σ_{coh} and σ_{inc}, which are determined by material constitutions. For example, the element hydrogen (H), probabaly the most important element in neutron scattering, has a σ_{inc} (80.2 barn) much greater than its σ_{coh} (1.8 barn) [34]. Therefore, neutron scattering measurements on hydrogen-rich systems, such as water and organic molecules, mainly probe the self dynamics of hydrogens. If other elements are crucial to the study, deuterated samples could be prepared since deuterium has a σ_{inc} (2.0 barn) comparable to its σ_{coh} (5.6 barn).

Besides these representations, another important formalism of the density-density correlations comes

from the inverse Fourier transform of intermediate scattering functions from reciprocal space to real space. This formalism, known as van Hove correlation functions [35, 36], shows a clear picture of densitiy-density correlations in space and time. The coherent van Hove correlation function is defined by

$$G(\mathbf{r},t) = \frac{1}{N}\left\langle \sum_{j,j'}^{N} \delta\left\{\mathbf{r} - \mathbf{r}_j(t) + \mathbf{r}_{j'}(0)\right\}\right\rangle, \tag{1.8}$$

where $G(\mathbf{r},t)d\mathbf{r}$ measures the probability of finding particles j in the shell volume $d\mathbf{r}$ at position $\mathbf{r}$ at time t given a particle j' at the origin at time 0. Similarly, the incoherent van Hove correlation funciton is given by the self part of $G(\mathbf{r},t)$,

$$G_s(\mathbf{r},t) = \frac{1}{N}\left\langle \sum_{j}^{N} \delta\left\{\mathbf{r} - \mathbf{r}_j(t) + \mathbf{r}_j(0)\right\}\right\rangle. \tag{1.9}$$

$G_s(\mathbf{r},t)d\mathbf{r}$ is a measure of the probability of finding a particle in the shell volume $d\mathbf{r}$ at position $\mathbf{r}$ at time t given itself at the origin at time 0. We summarize the relations among these density-density correlation functions expressed at different variable domains as follows,

$$S_{(s)}(\mathbf{k},\omega) \underset{\mathcal{F}^{-1}}{\overset{\mathcal{F} \text{ in time}}{\rightleftharpoons}} F_{(s)}(\mathbf{k},t) \underset{\mathcal{F}}{\overset{\mathcal{F}^{-1} \text{ in space}}{\rightleftharpoons}} G_{(s)}(\mathbf{r},t). \tag{1.10}$$

As shown in Figure 1.3, neutron scattering can probe various atomistic motions occuring at specific dynamic ranges and length scales. Its continuing applications to material studies will help advance our understanding of materials.

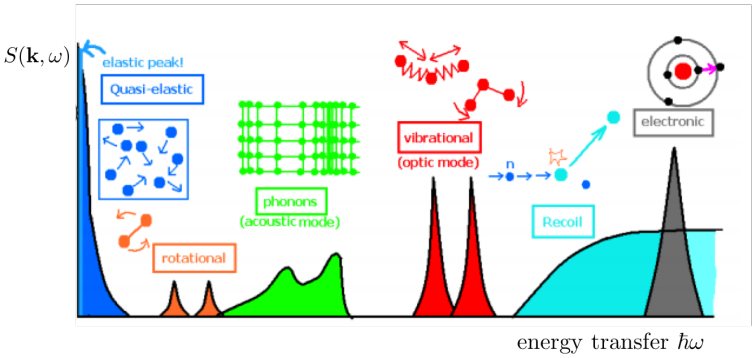

Figure 1.6: Illustration of dynamical modes measured at different ranges of the dynamic structure factor. (Adapted from Ref. [37])

Chapter 2

Relaxation Mode Analysis

The prevalence of large atomic displacements distinguishes liquids from solids. In crystalline solids, atoms are bounded to equilibrium lattice positions. Harmonic approximation offers a good treatment of strong interatomic interactions. In liquids, there exist significant atomic rearrangements and diffusive motions are dominant. Motivated by the success of normal modes analysis for crytalline solids, it is compelling to develop a counterpart for liquids.

In this chapter, we propose a relaxation mode analysis (RMA) for liquids by drawing analogy to normal mode analysis for crystalline solids. Under a similar framework that lattice vibrations in crystals can be decoupled into a distribution of normal modes in the frequency domain, complicated relaxations in liquids can be projected into a distribution of relaxation modes in the relaxation rate domain. This relaxation rate probability density function (RR-PDF) is related to the relaxation time probability density function (RT-PDF) and activation energy probability density function (AE-PDF). An activation-relaxation relation connecting these distribution functions is then established. This relation provides a possibility to extract the important statistics of activation barriers from experimentally measurable density-density correlation functions. Following this, we calculate the moments of the three distribution functions. Furthermore, we point out that RMA can be linked to the dynamic susceptibilities derived from linear response functions.

2.1 Relaxation Mode Analysis

RMA builds on the assumption that liquid motions are governed by various elementary diffusion processes. To describe an elementary diffusion, a Lagrangian [38] has been introduced as

$$\mathcal{L} = \int d\mathbf{r} \ \left[\alpha(\mathbf{r},t)\partial_t \rho(\mathbf{r},t) + D_l \nabla\rho(\mathbf{r},t)\cdot\nabla\alpha(\mathbf{r},t)\right], \tag{2.1}$$

where $\rho(\mathbf{r},t)$ is the atom density of a liquid and $\alpha(\mathbf{r},t)$ is a introduced conjugate field variable. The diffusion coefficient associated with a specific diffusion process is defined by D_l. Alternatively, using Hamiltonian

mechanics, a diffusion process can be described by a Hamiltonian [39, 40]

$$\mathcal{H} = \int \rho(\mathbf{r}, t)\ d\mathbf{r}, \tag{2.2}$$

which is based on a conserved quantity of motion, agreeing with the conservation law. Both descriptions yield a diffusion equation for $\rho(\mathbf{r}, t)$

$$\partial_t \rho(\mathbf{r}, t) = D_l \nabla^2 \rho(\mathbf{r}, t). \tag{2.3}$$

Conventionally, this diffusion equation can also be derived from the continuity equation

$$\partial_t \rho(\mathbf{r}, t) + \nabla \cdot \mathbf{j}(\mathbf{r}, t) = 0, \tag{2.4}$$

with the mass current $\mathbf{j}(\mathbf{r}, t)$ given by the Fick's law

$$\mathbf{j}(\mathbf{r}, t) = -D_l \nabla \rho(\mathbf{r}, t) \tag{2.5}$$

According to the Onsager regression hypothesis, the regression of microscopic spontaneous fluctuations in a equilibrium system follows the same law as the relaxation of macroscopic non-equilibrium disturbances [41]. Consequently, the self density-density correlation function $G_s(\mathbf{r}, t)$ satisfies

$$\partial_t G_s(\mathbf{r}, t) = D_l \nabla^2 G_s(\mathbf{r}, t), \tag{2.6}$$

Using Fourier transform, the diffusion equation in the reciprocal space is given by

$$\partial_t F_s(\mathbf{k}, t) = -D_l k^2 F_s(\mathbf{k}, t) = -z_l(\mathbf{k}) F_s(\mathbf{k}, t), \tag{2.7}$$

where $F_s(\mathbf{k}, t)$ is the self intermediate scattering function, and $z_l(\mathbf{k}) = D_l k^2$ denotes the relaxation rate. To emphasize, $F_s(\mathbf{k}, t)$ is a experimentally measurable quantity, e.g. from quasi-elastic or inelastic scattering experiments. The magnitude of wavevector transfer $\mathbf{k}$ is inversely proportional to the length scale probed. The k^2 dependence of relaxation rate $z_l(\mathbf{k})$ is usually only valid at very small $\mathbf{k}$ or long time limit. To describe liquid behaviors at larger $\mathbf{k}$ and intermediate time scales, Eq. (2.7) can be generalized to

$$\partial_t F_s(\mathbf{k}, t) = -D_l(\mathbf{k}) k^2 F_s(\mathbf{k}, t) = -z_l(\mathbf{k}) F_s(\mathbf{k}, t), \tag{2.8}$$

where $D_l(\mathbf{k})$ is the generalized k-dependent diffusion coefficient and $z_l(\mathbf{k}) = D_l(\mathbf{k})k^2$ is the generalized relaxation rate. The implication of this generalization is discussed in Appendix A.

Eq. (2.8) can be solved by introducing an inverse Laplace transform with respect to $F_s(\mathbf{k}, t)$, i.e.

$$F_s(\mathbf{k}, t) = \mathcal{L}\left[p(\mathbf{k}, z)\right] = \int_0^\infty dz\ e^{-zt} p(\mathbf{k}, z), \tag{2.9}$$

where $F_s(\mathbf{k}, t)$ and $p(\mathbf{k}, z)$ are Laplace transform pairs. The corresponding reverse transform is defined by the Bromwich integral

$$p(\mathbf{k}, z) = \mathcal{L}^{-1}\left[F_s(\mathbf{k}, t)\right] = \frac{1}{2\pi i}\int_{\gamma-i\infty}^{\gamma+i\infty} dt\ e^{zt} F_s(\mathbf{k}, t), \tag{2.10}$$

where the variable t is extended to complex domain, with its real part standing for a physical time. γ is a real number such that all singular points of $F_s(\mathbf{k}, t)$, if exist, locate in the left of vertical line $\mathrm{Re}[t] = \gamma$ in the complex plane. Replacing $F_s(\mathbf{k}, t)$ with Eq. (2.9), Eq. (2.8) becomes

$$\int dz\ e^{-zt}(z - z_l(\mathbf{k}))p(\mathbf{k}, z) = 0, \tag{2.11}$$

whose solution is given by

$$p(\mathbf{k}, z) = \delta(z - z_l(\mathbf{k})). \tag{2.12}$$

Analogous to the way that an eigen vibration mode in normal mode analysis is indicated by a delta-function in the vibration frequency ω domain, an elementary relaxation mode is represented by a delta-function in the relaxation rate z domain. Combining Eq. (2.9) and (2.12), the relaxation mode in time domain is given by single exponential decay

$$F_s(\mathbf{k}, t) = \exp[-z_l(\mathbf{k})t]. \tag{2.13}$$

For simple systems or liquids at high temperatures, single exponential decay given by Eq. (2.13) offers a good description of relaxation. However, for complex systems, a distribution of relaxation modes may exist. Due to simultaneous contributions from multiple relaxation modes, $F_s(\mathbf{k}, t)$ may deviate from simple exponential decay substantially and has no analytical expression. Any model that tries to quantify $F_s(\mathbf{k}, t)$ using a presumed number of relaxation modes becomes untenable. Under such circumstance, however, the inverse Laplace transform Eq. (2.9) still remains an effective method to distinguish distinct relaxation modes in the relaxation rate z domain. In other words, based on Eq. (2.9), $F_s(\mathbf{k}, t)$ can be considered as a superposition of elementary exponential relaxations with a distribution of characteristic relaxation rates.

This distribution is quantified by

$$p(\mathbf{k}, z) = \sum_l \delta(z - z_l(\mathbf{k})), \tag{2.14}$$

although the number of relaxation modes remains undetermined. For this reason, $p(\mathbf{k}, z)$ shows its physical meaning as a relaxation rate probability density function (RR-PDF), which provides important statistics of relaxation modes by Laplace-inverting $F_s(\mathbf{k}, t)$.

The RR-PDF $p(\mathbf{k}, z)$ in this relaxation mode analysis plays a similar role as the self dynamic structure factor in the normal mode analysis for solids. Both $S_s(\mathbf{k}, \omega)$ and $p(\mathbf{k}, z)$ are tranform pairs of $F_s(k, t)$ and provide important dynamical information in a similar manner. The former projects vibration modes in the frequency domain by inverse Fourier transform, while the latter distinguishes relaxation processes in the relaxation rate domain by inverse Laplace transform. As $S_s(\mathbf{k}, \omega)$ is the k-dependent density of states of vibration modes, in an analogous manner, $p(\mathbf{k}, z)$ can be interpreted as k-dependent density of states of relaxation modes.

This wavevector transfer $\mathbf{k}$ dependence of the RR-PDF $p(\mathbf{k}, z)$ controls the length scale at which a material system is probed. Due to the isotropic nature of liquids, this dependence usually relies on the magnitude of $\mathbf{k}$. The k value is inversely proportional to the length scale probed. Tuning k adjusts the probing resolution. This flexibility can be utilized to identify the governing relaxation modes at different length scales (see section 5.3). The exact manner in which $p(\mathbf{k}, z)$ depends on $\mathbf{k}$ is complicated. Nevertheless, at small k or short time limit, the dependences of $p(\mathbf{k}, z)$ on k and z can be decoupled, i.e.

$$\lim_{\substack{k\to 0 \\ \text{or } t\to 0}} p(\mathbf{k}, z) = \lim_{\substack{k\to 0 \\ \text{or } t\to 0}} \frac{k^2}{z^2} g(z), \tag{2.15}$$

where $g(z)$ is the inverse Laplace transform of velocity autocorrelation function

$$g(z) = \mathcal{L}^{-1}\left[\frac{\langle \mathbf{v}(0) \cdot \mathbf{v}(t)\rangle}{\langle \mathbf{v}(0)^2\rangle}\right]. \tag{2.16}$$

This relation can be verified using the cumulant expansion of $F_s(\mathbf{k}, t)$ [42, 43]. Analogous to the fact that Fourier transform of velocity autocorrelation function gives the density of states of vibration modes in solids, $g(z)$ can be interpreted as the k-independent density of states of relaxation modes in liquids.

For a clear comparison between the normal mode analysis for crystals and the relaxation mode analysis developed in this thesis for liquids, we summarize the key equations in Table 2.1.

Table 2.1: Comparisons between the normal mode analysis for crystals and the relaxation mode analysis for liquids

Materials	Crystals	Liquids
Physical motions	Lattice vibration	Diffusion/Relaxation
Lagrangian	$\mathcal{L}[\phi,\dot{\phi}]=\int d\mathbf{r}\left[\frac{\rho}{2}\dot{\phi}^2-\frac{1}{2}\rho(\mathbf{v}_l\cdot\nabla\phi)^2\right]$	$\mathcal{L}[\rho,\alpha]=\int d\mathbf{r}\ [\alpha\partial_t\rho+D_l\nabla\rho\cdot\nabla\alpha]$
Hamiltonian	$\mathcal{H}[\phi,\pi]=\int d\mathbf{r}\left[\frac{\pi^2}{2\rho}+\frac{1}{2}\rho(\mathbf{v}_l\cdot\nabla\phi)^2\right]$	$\mathcal{H}[\rho]=\int d\mathbf{r}\ \rho(\mathbf{r},t)$
Variable	$\phi(\mathbf{r},t)$	$\rho(\mathbf{r},t)=\sum_l\delta(\mathbf{r}-\mathbf{r}_l(t))$
Field equation	wave equation $\partial_{tt}\phi(\mathbf{r},t)=v_l^2\nabla^2\phi(\mathbf{r},t)$	diffusion equation $\partial_t\rho(\mathbf{r},t)=D_l\nabla^2\rho(\mathbf{r},t)$
Eq. of correlation function	$\partial_{tt}G_s(\mathbf{r},t)=v_l^2\nabla^2G_s(\mathbf{r},t)$	$\partial_tG_s(\mathbf{r},t)=D_l\nabla^2G_s(\mathbf{r},t)$
FT in space	$\partial_{tt}F_s(\mathbf{k},t)=-v_l^2k^2F_s(\mathbf{k},t)=-\omega_l^2(\mathbf{k})F_s(\mathbf{k},t)$ Generalization of $\mathbf{k}$ dependence $\partial_{tt}F_s(\mathbf{k},t)=-v_l^2(\mathbf{k})k^2F_s(\mathbf{k},t)=-\omega_l^2(\mathbf{k})F_s(\mathbf{k},t)$	$\partial_tF_s(\mathbf{k},t)=-D_lk^2F_s(\mathbf{k},t)=-z_l(\mathbf{k})F_s(\mathbf{k},t)$ Generalization of $\mathbf{k}$ dependence $\partial_tF_s(\mathbf{k},t)=-D_l(\mathbf{k})k^2F_s(\mathbf{k},t)=-z_l(\mathbf{k})F_s(\mathbf{k},t)$
FT and LT transform pairs	$F_s(\mathbf{k},t)=\mathcal{F}\left[S_s(\mathbf{k},\omega)\right]=\hbar\int d\omega\ e^{i\omega t}S_s(\mathbf{k},\omega)$ $S_s(\mathbf{k},\omega)=\mathcal{F}^{-1}\left[F_s(\mathbf{k},t)\right]=\frac{1}{2\pi\hbar}\int dt\ e^{-i\omega t}F_s(\mathbf{k},t)$	$F_s(\mathbf{k},t)=\mathcal{L}\left[p_s(\mathbf{k},z)\right]=\int_0^\infty dz\ e^{-zt}p_s(\mathbf{k},z)$ $p_s(\mathbf{k},z)=\mathcal{L}^{-1}\left[F_s(\mathbf{k},t)\right]=\frac{1}{2\pi i}\int_{c-i\infty}^{c+i\infty}dt\ e^{zt}F_s(\mathbf{k},t)$
Eigenmode in ω/z domain	$(\omega^2-\omega_l^2(\mathbf{k}))S_s(\mathbf{k},\omega)=0$ $\Longrightarrow S_s(\mathbf{k},\omega)=\delta(\omega\pm\omega_l(\mathbf{k}))$	$\int dz\ e^{-zt}(z-z_l(\mathbf{k}))p_s(\mathbf{k},z)=0$ $\Longrightarrow p_s(\mathbf{k},z)=\delta(z-z_l(\mathbf{k}))$
Eigenmode in time domain	$F_s(\mathbf{k},t)=\mathcal{F}\left[S_s(\mathbf{k},\omega)\right]=e^{\pm i\omega_l(\mathbf{k})t}$	$F_s(\mathbf{k},t)=\mathcal{L}\left[p_s(\mathbf{k},z)\right]=e^{-z_l(\mathbf{k})t}$
Schematic mode distribution	Incoherent dynamics structure factor $S_s(\mathbf{k},\omega)=\sum_l\delta(\omega\pm\omega_l(\mathbf{k}))$	relaxation rate probability density function $p_s(\mathbf{k},z)=\sum_l\delta(z-z_l(\mathbf{k}))$
Density of states	In the small $\mathbf{k}$ or short time limit, the $\mathbf{k}$ and ω dependences decouple $\lim_{\substack{k\to0\\ \text{or } t\to0}}S_s(\mathbf{k},\omega)=\lim_{\substack{k\to0\\ \text{or } t\to0}}\frac{k^2}{\omega^2}g(\omega)$ where $g(\omega)=\mathcal{F}^{-1}\left[\frac{\langle\mathbf{v}(0)\cdot\mathbf{v}(t)\rangle}{\langle\mathbf{v}(0)^2\rangle}\right]$ $g(\omega)=\lim_{\substack{k\to0\\ \text{or } t\to0}}S_s(\mathbf{k},\omega)\frac{\omega^2}{k^2}=\lim_{\substack{k\to0\\ \text{or } t\to0}}\mathcal{F}^{-1}[F_s(\mathbf{k},t)]\frac{\omega^2}{k^2}$	In the small $\mathbf{k}$ or short time limit, the $\mathbf{k}$ and z dependences decouple $\lim_{\substack{k\to0\\ \text{or } t\to0}}p_s(\mathbf{k},z)=\lim_{\substack{k\to0\\ \text{or } t\to0}}\frac{k^2}{z^2}g(z)$ where $g(z)=\mathcal{L}^{-1}\left[\frac{\langle\mathbf{v}(0)\cdot\mathbf{v}(t)\rangle}{\langle\mathbf{v}(0)^2\rangle}\right]$ $g(z)=\lim_{\substack{k\to0\\ \text{or } t\to0}}p_s(\mathbf{k},z)\frac{z^2}{k^2}=\lim_{\substack{k\to0\\ \text{or } t\to0}}\mathcal{L}^{-1}[F_s(\mathbf{k},t)]\frac{z^2}{k^2}$

2.2 Activation-Relaxation Relation

The RR-PDF $p(\mathbf{k},z)$ lays the foundation of RMA. Besides its physical importance clarified in last section, richer information can be derived from its connection to other distribution functions. For example, one can define a variable of relaxation time τ from the relaxation rate z,

$$z=1/\tau. \tag{2.17}$$

This relaxation time defines the characteristic time scale when the system relaxes back to its equilibrium status after a small perturbation. Using Eq. (2.17), we derived a relaxation time probability density function (RT-PDF)

$$p(\mathbf{k},\tau)=z^2p(\mathbf{k},z). \tag{2.18}$$

Besides, another important connection results from considering relaxation processes as activating events on the hypothesized energy landscape. The occurrence of relaxation requires overcoming certain activation energy barrier associated with configurational rearrangement. Therefore, the link between the relaxation rate and activation energy barrier can be establised using the Boltzmann factor, i.e.

$$z = z_0 \exp(-\frac{E_a}{k_B T}). \tag{2.19}$$

Consequently, the activation energy probability density function (AE-PDF) is given by

$$p(\mathbf{k}, E_a) = \frac{1}{k_B T} z p(\mathbf{k}, z) \tag{2.20}$$

where E_a is activation energy, $k_B T$ is thermal energy and z_0 is a pre-factor setting a baseline for activation barrier evaluation. Combining Eqs. (2.18) and (2.20), we arrive at an important relation among these distribution functions

$$k_B T p(\mathbf{k}, E_a) = \tau p(\mathbf{k}, \tau) = z p(\mathbf{k}, z). \tag{2.21}$$

We call this identity activation-relaxation relation (or A-R relation for short) because it establishes a link between activation events and relaxation processes. It is this A-R relation that provides a possibility to extract important statistics of activation barriers on the potential energy landscape from experimentally measurable quantity, namely, the intermediate scattering function $F_s(\mathbf{k}, t)$. In literature [44, 45, 46] the function $\tau p(\mathbf{k}, \tau)$ instead of $p(\mathbf{k}, \tau)$ has been used as a relaxation time distribution function on logarithm time scale mainly because the extracted distribution usually spans over many decades of relaxation time. However, the physical meaning of such practice remains ambiguous. From this A-R relation, we suggest that the importance of $\tau p(\tau)$ vs. logarithmic τ lies in its identity to the AE-PDF $p(\mathbf{k}, E_a)$ vs. E_a.

2.3 Moments of Distribution Functions

We devote this section to examine the moments of the three distribution functions mentioned in last section. These moments provide ensemble-averaged information of liquids that can be compared to experimental measurements.

In the first place, we consider the linear moments of the RR-PDF,

$$\int_0^\infty dz \; z^n p(\mathbf{k}, z) = (-1)^n \left[\frac{\partial^n}{\partial t^n} F_s(\mathbf{k}, t) \right]_{t=0}, \tag{2.22}$$

where the self intermediate scattering function $F_s(\mathbf{k},t)$ serves as a moment-generating function. The zero-th moment ensures that $p(\mathbf{k},z)$ is appropriately normalized since $F_s(\mathbf{k},t=0)=1$. The first moment defines the averaged relaxation rate. Second, we show that the linear moments of RT-PDF $p(\mathbf{k},\tau)$ are equal to the inverse moments of $p(\mathbf{k},z)$,

$$\begin{aligned}\int_0^\infty d\tau\ \tau^n p(\mathbf{k},\tau) &= \int_0^\infty dz\ \frac{1}{z^n}p(\mathbf{k},z)\\ &= \frac{1}{(n-1)!}\int_0^\infty dt\ t^{n-1}F_s(\mathbf{k},t).\end{aligned} \tag{2.23}$$

In particular, the first moment gives the well-known formula of averaged relaxation time

$$\begin{aligned}\langle\tau(\mathbf{k})\rangle &= \int_0^\infty d\tau\ \tau p(\mathbf{k},\tau)\\ &= \int_0^\infty dz\ \frac{p(\mathbf{k},z)}{z}\\ &= \int_0^\infty dt\ F_s(\mathbf{k},t)\end{aligned} \tag{2.24}$$

Third, based on Eq. (2.19), we show that the linear moments of $p(\mathbf{k},E_a)$ can be expressed as

$$\int_{-\infty}^\infty dE_a\ E_a^n p(\mathbf{k},E_a) = (k_BT)^n\int_0^\infty dz\ \left(\ln\frac{z_0}{z}\right)^n p(\mathbf{k},z) \tag{2.25}$$

By defining the logarithmic moments of $p(\mathbf{k},z)$ as

$$\langle(\ln z)^n\rangle = \int_0^\infty dz\ (\ln z)^n p(\mathbf{k},z), \tag{2.26}$$

we obtain the k-dependent averaged activation energy from the first moment

$$\langle E_a(\mathbf{k})\rangle = \int_{-\infty}^\infty dE_a\ E_a p(\mathbf{k},E_a) = k_BT\left[\ln z_0 - \langle\ln z\rangle\right], \tag{2.27}$$

and the variance of activation barriers from the second moment

$$\begin{aligned}\sigma^2[E_a(\mathbf{k})] &= \int_{-\infty}^\infty dE_a\ (E_a-\langle E_a\rangle)^2 p(\mathbf{k},E_a)\\ &= (k_BT)^2\left[\langle(\ln z)^2\rangle - \langle\ln z\rangle^2\right].\end{aligned} \tag{2.28}$$

Note that $\langle E_a(\mathbf{k})\rangle = 0$ when $\ln z_0 = \langle\ln z\rangle$. Thus $k_BT\ln z_0$ sets a base line for the evaluation of $\langle E_a(\mathbf{k})\rangle$. Unlike $\langle E_a(\mathbf{k})\rangle$, the variance $\sigma^2[E_a(\mathbf{k})]$ is independent of z_0. These expressions provide basic quantifications of activation barriers on the energy landscape.

2.4 Link to Linear Response Susceptibilities

Linear response theory [47] has been an important approach in describing how a material system responds to weak perturbations caused by external fields or spontaneous fluctuations. In this section, we show that RMA can be linked to the linear response formalism. This link not only extends practical approaches that have access to the RR-PDF $p(\mathbf{k}, z)$, but also suggests a possibility of applying the framework of RMA to quantify other relaxation phenomena.

In the context of structural relaxation, we start with a response function of density fluctuations defined by the self intermediate scattering function [47]

$$\chi(\mathbf{k}, t) = -\beta \frac{\partial F_s(\mathbf{k}, t)}{\partial t} \tag{2.29}$$

where $\beta = 1/k_B T$, and k_B is the Boltzmann constant. Using Eq. (2.9) and (2.29), the Laplace transform pair of $\chi(\mathbf{k}, t)$ is given by

$$\begin{aligned}
\chi(\mathbf{k}, \tilde{z}) &= \int_0^\infty dt\ e^{i\tilde{z}t} \chi(\mathbf{k}, t) \\
&= -\beta \int_0^\infty dt\ e^{i\tilde{z}t} \frac{\partial F_s(\mathbf{k}, t)}{\partial t} \\
&= \beta \int_0^\infty dt\ e^{i\tilde{z}t} \left[\int_0^\infty dz\ e^{-zt} z p(\mathbf{k}, z) \right] \\
&= \beta \int_0^\infty dz\ z p(\mathbf{k}, z) \left[\int_0^\infty dt\ e^{-(z - i\tilde{z})t} \right] \\
&= \beta \int_0^\infty dz\ p(\mathbf{k}, z) \frac{z}{z - i\tilde{z}},
\end{aligned} \tag{2.30}$$

where $\tilde{z} = \omega + i\varepsilon$ is a complex variable. Taking the $\varepsilon \to 0$ limit of function $\chi(\mathbf{k}, \tilde{z})$ gives the dynamic susceptibility

$$\begin{aligned}
\chi(\mathbf{k}, \omega) &= \lim_{\varepsilon \to 0} \chi(\mathbf{k}, \tilde{z} = \omega + i\varepsilon) \\
&= \beta \int_0^\infty dz\ p(\mathbf{k}, z) \frac{z^2 + i\omega z}{z^2 + \omega^2}.
\end{aligned} \tag{2.31}$$

The real and imaginary parts are given, respectively, by

$$\chi'(\mathbf{k}, \omega) = \mathrm{Re}[\chi(\mathbf{k}, \omega)] = \beta \int_0^\infty dz\ p(\mathbf{k}, z) \frac{z^2}{z^2 + \omega^2}, \tag{2.32}$$

$$\chi''(\mathbf{k}, \omega) = \mathrm{Im}[\chi(\mathbf{k}, \omega)] = \beta \int_0^\infty dz\ p(\mathbf{k}, z) \frac{\omega z}{z^2 + \omega^2}. \tag{2.33}$$

One can verify that these two expressions satisfy the Kramers-Kronig relation [47].

Furthermore, it is known that the dynamic structure factor measured from scattering experiments is closely related to the imaginary part of dynamic susceptibility $\chi''(\mathbf{k},\omega)$. This relation can also be derived using RMA. As mentioned in section 1.3, the self dynamic structure factor $S_s(\mathbf{k},\omega)$ is the Fourier transform of self intermediate scattering function. Using Eq. (2.9), $S_s(\mathbf{k},\omega)$ can be written as

$$\begin{aligned} S_s(\mathbf{k},\omega) &= \frac{1}{2\pi\hbar}\int_{-\infty}^{\infty} dt\ e^{-i\omega t} F_s(\mathbf{k},|t|) \\ &= \frac{1}{\pi\hbar}\int_0^{\infty} dt\ \cos(\omega t)\left[\int_0^{\infty} dz\ e^{-zt} p(\mathbf{k},z)\right] \\ &= \frac{1}{\pi\hbar}\int_0^{\infty} dz\ p(\mathbf{k},z)\left[\int_0^{\infty} dt\ e^{-zt}\cos(\omega t)\right] \\ &= \frac{1}{\pi\hbar}\int_0^{\infty} dz\ p(\mathbf{k},z)\frac{z}{z^2+\omega^2} \end{aligned} \tag{2.34}$$

From Eq. (2.33) and (2.34), we recover the relation between $\chi''(\mathbf{k},\omega)$ and $S_s(\mathbf{k},\omega)$, i.e.

$$S_s(\mathbf{k},\omega) = \frac{1}{\beta\pi\hbar}\frac{\chi''(\mathbf{k},\omega)}{\omega}, \tag{2.35}$$

which has been known as an important consequence of the fluctuation-dissipation theorem [47].

Chapter 3

Numerical Methods for Inverse Laplace Transform

As indicated by Eq. (2.9), inverse Laplace transform (ILT) plays a critical role in extracting the important statistics of relaxation modes and activation barriers from the intermediate scattering function $F_s(\mathbf{k}, t)$. Although an analytical inversion formula utilizing complex integral (Eq. (2.10)) exists, its applicability is limited due to the lack of analytical expression of $F_s(\mathbf{k}, t)$. Moreover, $F_s(\mathbf{k}, t)$ obtained from computer simulations or experiments is typically known in the form of discrete numeric data, located on the real axis of time t. The numeric data may be contaminated by systematic or environmental noise to certain degrees. Under these circumstances, numerical ILT needs to be carried out carefully.

Over the past few decades, various numerical methods for ILT has been proposed and discussed in journals [48, 49, 50, 51] and a book by Cohen [52]. Besides, an extensive bibliography of over 1000 papers on numerical methods for ILT and their applications has been maintained by Valko and Vojta [53]. In this chapter, we divide the numerical methods for ILT into three main categories in terms of the possessed knowledge of the inputted intermediate scattering function $F_s(\mathbf{k}, t)$. Some important methods in each category are highlighted. To simplify the notations, we drop the $\mathbf{k}$ dependence in Eq. (2.9) and rewrite the ILT of $F_s(\mathbf{k}, t)$ as follows

$$F_s(t) = \int_0^\infty dz\ p(z)e^{-zt}. \tag{3.1}$$

3.1 Inversion of Analytical Functions

In the first category where the analytical expression of input $F_s(\mathbf{k}, t)$ is known or presumed, the scope of accessible data can be extended to the complex plane. Besides, an analytical function is free of noise. Accordingly, numerical ILT can be accomplished by taking advantage of the Bromwich inversion integral along some specific path on the complex plane. Important approaches that fit in this category include the Euler algorithm (a Fourier-series method with Euler summation) [54, 50] and the Talbot algorithm (a method utilizing the deformation of the Bromwich integral path) [55, 56]. We summarize these two algorithms in the following:

- **The Euler algorithm** [51]:

$$p(z) = \frac{10^{M/3}}{z} \sum_{k=0}^{2M} \eta_k \mathrm{Re}\left[F_s\left(\frac{\beta_k}{z}\right)\right], \tag{3.2}$$

where

$$\beta_j = \frac{M\ln(10)}{3} + ik\pi, \quad \eta_k \equiv (-1)^j \xi_k \tag{3.3}$$

with $i = \sqrt{-1}$ and

$$\begin{aligned} \xi_0 &= \frac{1}{2}, \quad \xi_{2M} = \frac{1}{2M}, \\ \xi_k &= 1, \quad 1 \le k \le M, \\ \xi_{2M-k} &= \xi_{2M-k+1} + 2^{-M}\binom{M}{k}, \quad 0 < k < M. \end{aligned} \tag{3.4}$$

In computation, if j significant digits in the result are desired, one can choose M as the integer $\lceil 1.7j \rceil$. Accordingly, a system precision of at least M is required.

- **The Talbot algorithm** [51]:

$$p(z) = \frac{2}{5z} \sum_{k=0}^{M-1} \mathrm{Re}\left[\gamma_k F_s\left(\frac{\delta_k}{z}\right)\right], \tag{3.5}$$

where

$$\begin{aligned} \delta_0 = \frac{2M}{5}, \quad \delta_k = \frac{2k\pi}{5}\left[\cot\left(\frac{k\pi}{M}\right) + i\right], \quad 0 < k < M; \\ \gamma_0 = \frac{1}{2}e^{\delta_0}, \quad \gamma_k = \left[1 + i\left(\frac{k\pi}{M}\right)\left(1 + \cot^2\left(\frac{k\pi}{M}\right)\right) - i\cot\left(\frac{k\pi}{M}\right)\right]e^{\delta_k}, \quad 0 < k < M. \end{aligned} \tag{3.6}$$

and $i = \sqrt{-1}$. Like the Euler algorithm, if j significant digits are desired, one can choose M as the integer $\lceil 1.7j \rceil$ and the machine precision at least M.

Instead of integrating the complex integral, some algorithms have been proposed to utilize only real-valued data located on the real axis, such as the Gaver-Stefest algorithm described as follows:

- **The Gaver-Stehfest algorithm** [51]:

$$p(z) = \frac{\ln(2)}{z} \sum_{k=1}^{2M} \xi_k F_s\left(\frac{k\ln(2)}{t}\right), \tag{3.7}$$

where

$$\xi_k = (-1)^{M+k} \sum_{j=\lfloor (k+1)/2 \rfloor}^{\min\{k,M\}} \frac{j^{M+1}}{M!} \binom{M}{j} \binom{2j}{j} \binom{j}{k-j}, \tag{3.8}$$

and $\lfloor x \rfloor$ means the greatest integer that is not greater than x. In computation, if j significant digits are desired, one can choose M as $\lceil 1.1j \rceil$ and set the system precision at least $\lceil 2.2M \rceil$.

Compared to the last two algorithms, the Gaver-Stehfest algorithm requires a higher machine precision in implementation. The benifit gained is that only real numbers are needed in the calculation. These methods serve as important tools for testing empirical model functions.

3.2 Inversion of Clean Discrete Data

It is more often the case that the input $F_s(\mathbf{k}, t)$ is only known as tabular numeric data and its analytical form is lacking. Depending on the degree of noise in the data, we classify the numerical methods for ILT of discrete data into the other two categories. When the input data are available in high precision, direct inversion is still possible, for example, by using the Gaver-Stehfest algorithm with data interpolated to specific nodes. In addition, indirect inversion approaches such as applying numerical fitting techniques to Eq. (3.1) can be employed to solve the problem. By approximating Eq. (3.1) with certain quadrature rule over a finite range, one can construct a least squares problem that minimizes

$$\begin{aligned} \chi^2_{lsq} &= \sum_{i=1}^{N_y} \left[F_s(t_i) - \sum_{j=1}^{N_x} c_j e^{-z_j t_i} p(z_j) \right]^2 \\ &= ||\mathbf{y} - \mathbf{C}\mathbf{x}||_2^2, \end{aligned} \tag{3.9}$$

where c_j is the quadrature weight, and coefficients $c_j e^{-z_j t_i}$ form the $N_y \times N_x$ matrix $\mathbf{C}$. The $N_y \times 1$ vector $\mathbf{y}$ contains input data $F_s(t)$, and vector $\mathbf{x}$ ($N_x \times 1$) is the seeking solution $p(z)$ evaluated at finite grid points z_j within an interval $[z_{\min}, z_{\max}]$. Many optimization algorithms can be applied to solve this type of ordinary least squares problem (see Ref. [57] or Chapter 3 and 6 of Ref. [58]).

3.3 Inversion of Noisy Discrete Data

In the third category, we consider the inversion of discrete data contaminated by considerable noise. This inverse problem is generally ill-posed, and becomes ill-conditioned when translated to numerical representation. There exist a family of solutions satisfying Eq. (3.1) within error and they differ from each other

significantly [59]. The ordinary least squares method alone doesn't alleviate the ill-conditioning represented by the singularity of coefficient matrix $\mathbf{C}$ in Eq. (3.9). As a result, the obtained solution may suffer strong oscillations. Thus additional techniques and constraints imposing prior knowledge or simplicity become critical for seeking the optimal solution. One useful approach is to introduce additional regularization terms penalizing undesired features based on prior knowledge or principle of simplicity. Instead of minimizing conventional χ^2_{lsq} such as Eq. (3.9), a regularized least squares problem intends to minimize

$$\chi^2 = \chi^2_{lsq} + \chi^2_{reg}, \tag{3.10}$$

where χ^2_{reg} incorporates additional regularization terms (regularizors) added to any specific problem. In general, multiple regularizors may be applied independently, i.e.

$$\chi^2_{reg} = \sum_l \lambda_l W_l \left[p(z)\right], \tag{3.11}$$

where $W_l[p(z)]$ is a regularization functional of $p(z)$ that specifies the l-th regularizor, and λ_l is the corresponding regularization parameter. The chosen form of $W[p(z)]$ determines the effectiveness of regularization, while the regularization parameter λ specifies the penalty strength. Depending on the prior knowledge possessed or undesired features to suppress, $W[p(z)]$ may vary case by case.

In the following, we point out some regularizors that have been commonly used. First of all, regularizors that penalize the derivatives of the solution help suppress different features in the solution, such as large magnitude (zero derivative), large slope (first derivative), and large curvature (second derivative). Penalizing the first derivative and the second derivative both contribute to removing strong oscillations and thus tend to smooth the solution. These "linear" regularization functionals can be summarized as

$$\begin{aligned} W[p(z)] &= \int_{z_{\min}}^{z_{\max}} \left| \frac{d^n p}{dz^n} \right|^m \, dz \\ &= ||\mathbf{Rx}||_m^m, \end{aligned} \tag{3.12}$$

where n = 0, 1, 2 are commonly adopted, and m = 1, 2 specifies L^1-norm and L^2-norm, respectively. The second identity in Eq. 3.12 results from applying some numerical quadrature rule to the integral and approximating the derivative by finite difference. The $N_{reg} \times N_x$ matrix $\mathbf{R}$ is determined by the quadrature rule and the order of derivative simultaneously. For instance, if the trapezoidal quadrature rule is used, $\mathbf{R}$

reduces to a square identity matrix for $n = 0$. For $n = 1$, it becomes an $(N_x + 2) \times N_x$ matrix

$$\mathbf{R} = \begin{bmatrix} 1 & & & \\ 0 & 1 & & \\ -1 & 0 & \ddots & \\ & -1 & \ddots & 1 \\ & & \ddots & 0 \\ & & & -1 \end{bmatrix}; \tag{3.13}$$

for $n = 2$,

$$\mathbf{R} = \begin{bmatrix} 1 & & & \\ -2 & 1 & & \\ 1 & -2 & \ddots & \\ & 1 & \ddots & 1 \\ & & \ddots & -2 \\ & & & 1 \end{bmatrix} \tag{3.14}$$

Here two additional nodes are enforced to zeros on each side outside $[z_{\min}, z_{\max}]$, which is usually a good practice when the solution only locates at finite range. If this is not desired, the first two rows and the last two rows can be removed. Some constants resulting from the finite difference are also ignored since they can be absorbed into the regularization parameter λ.

If L^2-norm (m = 2) is adopted in Eq. (3.12), the resulting regularization is called Tikhonov regularization or ridge regression [60]. It is effective in imposing smoothness in the solution. In the other case that L^1-norm (set m = 1) is used , it is known as LASSO (least absolute shrinkage and selection operator) regression [61, 62]. For LASSO, penalizing different derivatives can be considerd from the geometrical perspective. It

intends to penalize the area underneath the solution curve for $n = 0$, and the approximate string length of the solution curve for $n = 1$. The combination of ridge regression and LASSO with appropriately adjusted weights yields another important regularization formulation known as the elastic net method [63].

Besides "linear" regularizors, another useful regularization approach derived from information theory is called maximum entropy method [64, 65]. It has been widely applied to inverse problems such as image reconstruction [66, 67], natural language processing [68], as well as model extractions in physical science [69, 70, 71, 72]. The spirit behind this method is to pick a solution that is most objective with respect to missing information in the data by maximizing the information entropy conveyed by the solution. This regularization functional is defined by

$$W[p(z)] = -S[p(z)] = \int_{z_{\min}}^{z_{\max}} p(z) \ln p(z) \; dz \tag{3.15}$$

where $S[p(z)]$ is the information entropy. Non-negative constraint on the solution is implicitly imposed by the maximum entropy method.

A complete regularizor depends on not only the regularization functional but also the value of regularization parameter. A very small value doesn't help address the ill-conditioned inverse problem, while a very large value may over-bias the original problem and the sought solution may be oversmoothed. Several strategies have been proposed to pick the regularization parameter, including the discrepancy principle [73], cross-validation [74], and L-curve criterion [75, 76]. Their effectiveness varies from case to case. It still remains a challenge to develop a universal strategy. We show the effects of the regularization parameter on the obtained solution in section 4.4.

Once the regularizors are specified, the resulting regularized least squares problem is ready to be solved by optimization algorithms. At this stage, additional constraints, such as linear equality or inequality, can be further enforced on the solution. In this thesis, the solution of Laplace inversion being sought is a nonnegative probability density function, which implies that a nonnegative constraint $\mathbf{x} \geq 0$ is desired.

In this thesis, we adopt the linear regularizors together with the nonnegative constraint to help carry out numerical ILT. In other words, we intend to solve a regularized least squares problem that minimizes

$$\chi^2 = ||\mathbf{y} - \mathbf{C}\mathbf{x}||_2^2 + \lambda ||\mathbf{R}\mathbf{x}||_m^m \tag{3.16}$$

under the nonnegative constraint $\mathbf{x} \geq 0$. For the case of ridge regression ($m = 2$), a CONTIN algorithm [59, 77] has been widely applied to extract the solution. We summarize this CONTIN algorithm in Appendix B. Alternatively, a universal approach for solving both ridge regression ($m = 2$) and LASSO regression ($m = 1$)

is further transforming the problem to quadratic programming. Quadratic programming is a category of optimization problems aiming to find a solution $\mathbf{u}$ that minimizes the quadratic function

$$\frac{1}{2}\mathbf{u}^T\mathbf{Q}\mathbf{u} + \mathbf{f}^T\mathbf{u}, \tag{3.17}$$

where the notation T denotes transpose. The solution $\mathbf{u}$ may be subject to linear constraint(s), e.g.

$$\mathbf{A}_{\text{ieq}}\mathbf{u} \leq \mathbf{b}_{\text{ieq}}, \tag{3.18a}$$

$$\mathbf{A}_{\text{eq}}\mathbf{u} = \mathbf{b}_{\text{eq}}, \tag{3.18b}$$

$$\mathbf{b}_{\text{lower}} \leq \mathbf{u} \leq \mathbf{b}_{\text{upper}}. \tag{3.18c}$$

Using the notations in Eqs. (3.16), (3.17) and (3.18), we summarize the mapping from the regularized least squares problem with nonnegtaive constraint to a constrained quadratic programming problem in the following:

- ridge regression ($m = 2$):

$$\begin{cases} \mathbf{u} = \mathbf{x} \\ \mathbf{H} = \mathbf{2C}^T\mathbf{C} + 2\lambda\mathbf{R}^T\mathbf{R},\ \mathbf{f}^T = -2\mathbf{y}^T\mathbf{C} \\ \mathbf{b}_{\text{lower}} = \mathbf{0} \end{cases} \tag{3.19}$$

- LASSO regression ($m = 1$):

$$\begin{cases} \mathbf{u} = (\mathbf{x}^T \quad \mathbf{v}_+^T \quad \mathbf{v}_-^T)^T, \\ \mathbf{v} = \mathbf{R}\mathbf{x},\ \mathbf{v}_+ = \max\{\mathbf{v}, 0\},\ \mathbf{v}_- = \max\{-\mathbf{v}, 0\} \\ \mathbf{H} = \begin{pmatrix} 2\mathbf{C}^T\mathbf{C} & & \\ & \mathbf{O} & \\ & & \mathbf{O} \end{pmatrix},\ \mathbf{f}^T = (-2\mathbf{y}^T\mathbf{C} \quad \lambda\mathbf{1}^T \quad \alpha^2\mathbf{1}^T) \\ \mathbf{A}_{eq} = (\mathbf{R} \quad -\mathbf{I} \quad \mathbf{I}), \quad \mathbf{b}_{eq} = \mathbf{0}, \quad \mathbf{b}_{\text{lower}} = \mathbf{0} \end{cases} \tag{3.20}$$

Quadratic programmming can be solved by various approaches, such as active set method [78] and interior point algorithm [79].

To summarize this chapter, numerical methods for ILT can be practically divided to three categories,

depending on the available knowledge of the input. First, if the analytical form of the input $F_s(t)$ is known, multiple algorithms, such as the Euler algorithm and the Talbot algorithm, can be used to approximate the Bromwich inversion integral. Second, if the input $F_s(t)$ is only known as tabular real-valued data with negligible noise, the Gaver-Stehfest algorithm may be applied. More generally, the Laplace inversion can also be solved by constructing an ordinary least squares problem. In the third case where considerable noises contaminate the input data, the constructed ordinary least squares problem becomes highly ill-conditioned and additional regularization techniques and (or) constraints are needed to help improve stability in the search of an optimal solution. Common regularization approaches include the ridge regression and LASSO regression (linear regularization) as well as the maximum entropy method (nonlinear regularization). If a linear regularizor is employed, the resulting regularized problem such as Eq. (3.16) can be further mapped to a quadratic programming problem and then solved.

The RMA approach proposed in this thesis typically relies on inverting discrete data of the intermediate scattering function collected from either computer simulations or experiments. Therefore, we applied the numerical method of the third caterogory discussed in this chapter to carry out the analyses thorought this thesis. Specifically, the Laplace inversion from $F_s(\mathbf{k}, t)$ to $p(\mathbf{k}, z)$ was first formulated as a ridge regression problem, which was further transformed to a quadratic programming problem and then solved by the active set method.

Chapter 4

Demonstrations of Relaxation Mode Analysis

For the purpose of demonstration, we apply RMA to examine three examples in this chapter, i.e. exponential relaxation, stretched exponential relaxation, and relaxation process arising from Gaussian-distributed activation barriers. As mentioned at the end of last chapter, the Laplace inversion from $F_s(\mathbf{k}, t)$ to $p(\mathbf{k}, z)$ was first formulated as a ridge regression problem and then solved by utilizing quadratic programming algorithms. The solution obtained relies on the choice of regularization parameter used in the inversion. Thus, how the regularization parameter affects the obtained solution is examined at the end of this chapter.

4.1 Exponential Relaxation

Exponential decay is an important law governing many physical phenomena [80]. In the framework of RMA, it represents the elementary relaxation mode in liquids. A characteristic relaxation time can be defined from the time period required for the function intensity to reduce to $1/e$ of its initial value. The inverse of this relaxation time defines the relaxation rate. In the presence of multiple exponential relaxations, the relaxation time (rate) given by the $1/e$ definition is an averaged quantity due to multiple simultaneous contributions. Individual contribution of each mode becomes ambiguous. To address this limitation, in this first example, we show that a combination of multiple exponential relaxations can be decoupled using RMA.

Consider a special case of Eq. (3.1) that there exists only two relaxation modes

$$p(z) = c\delta(z - z_1) + (1 - c)\delta(z - z_2), \tag{4.1}$$

where each mode has a characteristic relaxation rate z_1 and z_2, respectively. The fraction c ($0 < c < 1$) specifyies the contribution from each mode. In this situation, the intermediate scattering function reduces to a summation of two exponential decays

$$F_s(t) = c \exp(-z_1 t) + (1 - c) \exp(-z_2 t). \tag{4.2}$$

In the test, the input data of $F_s(t)$ was first generated from Eq. (4.2) (taking $z_1 = 1$, $z_2 = 0.1$ and $c = 0.5$) and then fed into a in-house program for ILT using the numerical method described at the end of last chapter. As pointed out in Section 2.2, the A-R relation provides an important connection among the three distribution functions: AE-PDF, RT-PDF, and RR-PDF. Thus in this thesis, we focus on the A-R relation when presenting numerical results of RMA. In Fig. 4.1(a1), we show the input $F_s(t)$ together with numerically extracted A-R relation. The analytical solution (Eq. (4.1)) is also plotted. The good agreement between numerical and analtyical solution confirms the validity of the numerical method applied. The extracted curve of the A-R relation can be interpreted in three ways, depending on the variable in concern. For example, the curve shows the important distribution of activation energy barriers when one interprets it as $k_BTp(E_a)$ vs. ΔE_a, where $\Delta E_a = E_a - k_BT \ln z_0$ according to Eq. (2.19). Alternatively, the curves also defines the distribution of relaxation times ($\tau p(\tau)$ vs. τ) and the distribution of relaxation rates ($zp(z)$ vs. z).

Besides, Figure 4.1(a2) shows another case similar to Fig. 4.1(a1) except that appreciable white Gaussian noise was added to the input $F_s(t)$ data, achieving a signal-to-noise ratio of 35 dB. Despite some discrepancies between the numerical and analytical solution, it is clear that the numerical method is able to reconstruct the two singular δ functions reliably. Note that the exact shape of A-R relation relies on the choice of regularization parameter. In this thesis, we only focus on those aspects that are consistent across different regularization parameters.

This example also illustrates the common practice of fitting quasi-elastic neutron scattering data (the dynamic structure factor) with multiple Lorentzians. Combining Eq. (4.1) with (2.34), the self dynamic structure factor is given by

$$S_s(\omega) = \frac{1}{2\pi\hbar}\left[c\frac{z_1}{z_1^2+\omega^2} + (1-c)\frac{z_2}{z_2^2+\omega^2}\right]. \tag{4.3}$$

One Lorentzian function in the frequency domain stands for one relaxation mode. RMA generalizes the practice of multiple Lorentizian fitting without presuming the number of relaxation modes. This extension makes RMA a promising approach to analyze quasi-elastic and inelastic neutron scattering data from the measurements of complex systems.

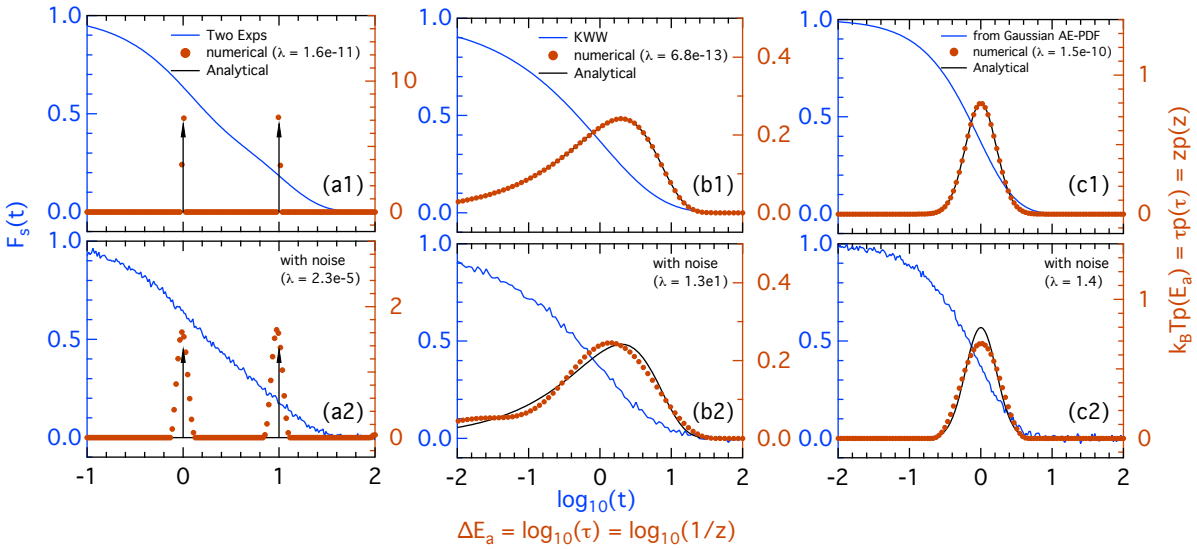

Figure 4.1: Application of RMA to three representative intermediate scattering functions: (a1) Summation of two exponential decays given by Eq. (4.2), with $z_1 = 1$ and $z_2 = 0.1$. (b1) KWW (stretched exponential) function given by Eq. (4.4), where $\tau_K = 1$ and $\beta = 0.5$. (c1) Relaxation function integrated from a Gaussian AE-PDF given by Eq. (4.10), where $\mu = E_0$, $\sigma = \frac{1}{2}k_BT$ (namely $\mu' = 0$, $\sigma' = \frac{1}{2}$ in Eq. (4.11)). (a2), (b2), and (c2) use the same parameters as (a1), (b1), and (c1), respectively, except that appreciable white Gaussian noises were added to the input data (achieving a signal-noise-ratio of 35 dB). In each case, the blue curve is the intermediate scattering function. The numerical solution is plotted as filled circles, and analytical solutions are black curves. For clarity, the units of variables are not shown explicitly in the figure. ΔE_a has the unit of $\ln(10)k_BT$. t and τ has the dimension of time, and z has the dimension of inverse time. ΔE_a is related to the absolute activation energy E_a by $\Delta E_a = E_a - k_BT \ln z_0$. The regularization parameter λ is shown for each case in the plot.

4.2 Stretched Exponential Relaxation

Nonexponential decay characterizes another important type of relaxation behaviors of complex systems under extreme conditions. One of the most important nonexpoential form is the stretched exponential relaxation

$$F_s(t) = \exp\left[-\left(\frac{t}{\tau_K}\right)^{\beta}\right], \tag{4.4}$$

where τ_K defines the characteristic relaxation time and the stretching exponent β ranges from 0 to 1. This empirical function has been known as Kohlrausch-Williams-Watts (KWW) model [81, 82] and widely used to fit experimental data from nuclear magnetic resonance, dielectric relaxation, dynamic light scattering, quasi-elastic neutron scattering, etc. The analytical formula of Laplace inversion of this stretched exponential

decay was first obtained by Humbert [83] in the form of series expression

$$p(z) = \frac{\tau_K}{\pi} \sum_{n=0}^{\infty} \frac{(-1)^{n+1}}{n!} \sin(n\beta\pi) \frac{\Gamma(n\beta+1)}{(z\tau_K)^{n\beta+1}}, \tag{4.5}$$

where $\Gamma(\cdots)$ is the Gamma function. An alternative inverse formula of integral form was given by the Pollard's relation [84],

$$p(z) = \frac{\tau_K}{\pi} \int_0^{\infty} \exp(-z\tau_K u) \exp\left[-u^{\beta}\cos(\beta\pi)\right] \sin\left[u^{\beta}\sin(\beta\pi)\right] \; du. \tag{4.6}$$

Moreover, Berberan-Santos [85, 86] found a family of equivalent inversion integrals, which can be expressed as any normalized linear combination of

$$p(z) = \frac{2\tau_K}{\pi} \int_0^{\infty} \exp\left[-u^{\beta}\cos(\frac{\beta\pi}{2})\right] \cos\left[u^{\beta}\sin(\frac{\beta\pi}{2})\right] \cos(z\tau_K u) du \tag{4.7}$$

and

$$p(z) = \frac{2\tau_K}{\pi} \int_0^{\infty} \exp\left[-u^{\beta}\cos(\frac{\beta\pi}{2})\right] \sin\left[u^{\beta}\sin(\frac{\beta\pi}{2})\right] \sin(z\tau_K u) du. \tag{4.8}$$

These formulas don't reduce to elementary functions for a general β. The only exception is when $\beta = 0.5$,

$$p_{s,0.5}(z) = \frac{1}{\sqrt{4\pi z^3 \tau_K}} \exp\left(\frac{1}{4z\tau_K}\right) \tag{4.9}$$

In this section we show an example with $\beta = 0.5$.

Figure 4.1(b1) demonstrates the application of RMA to the stretched exponential function 4.4. The stretching exponent $\beta = 0.5$ is chosen so that the analytical solution is available for comparison. Again, we obtained an excellent agreement between the numerical solution and the analytical solution. Despite the shape similarity between the input $F_s(t)$ in Fig. 4.1(a1) and 4.1(b1), remarkable differences were observed in the obtained A-R relations. Unlike the exponential relaxation, stretched exponential relaxation is associated with a broad asymmetric distribution of activation energies or relaxation times. A long tail was observed on the low activation energy side. Moreover, we show in Fig 4.1(b2) another similar case except that noisy data (with signal-noise-ratio 35 dB) are used as input. The numerical method still works reliably in this high noise level.

4.3 Gaussian Activation

In the third example, we consider activation energy barriers that satisfy a Gaussian distribution. In other words, the AE-PDF follows

$$p(E_a) = \frac{1}{\sqrt{2\pi}\sigma} \exp\left[-\frac{(E_a - \mu)^2}{2\sigma^2}\right], \tag{4.10}$$

where μ and σ denote the mean and variance, respectively. Using Eq. (2.19) and (2.21), this distribution corresponds to a log-normal function of RR-PDF, i.e.

$$p(z) = \frac{1}{z}\frac{1}{\sqrt{2\pi}\sigma'} \exp\left[-\frac{(\ln z + \mu')^2}{2\sigma'^2}\right] \tag{4.11}$$

where $\mu' = \mu/k_BT - \ln z_0 = (\mu - E_0)/k_BT$ and $\sigma' = \sigma/k_BT$. Unlike the previous two examples, there is no analytical expression for $F_s(t)$ in this case. Thus in this test, the data of $F_s(t)$ was first obtained from numerical integration of Eq. (2.9), and was then Laplace-inverted to compare with the analytical solution Eq. (4.10). Figure 4.1(c1) shows this comparison. In Fig. 4.1(c2), white Gaussian noises were further added to the $F_s(t)$ data before the numerical ILT was carried out. In both cases, the analytical solution was reliably recovered by the numerical solutions.

4.4 The Effects of Regularization Parameter

In the three examples shown in previous sections, we observed good agreements between the numerical solutions and the analytical solutions using certain regularization parameters. We primarily use the L-curve criterion [75, 76] to determine the value of regularization parameter. The idea is to pick the regularization parameter corresponding to the point of maximum curvature in the log-log plot of χ_{reg} vs. χ_{lsq}, or the so-called "L-curve". In some cases, however, the L-curve doesn't exhibit an "L" shape and thus this strategy fails to predict an optimal regularization parameter. Under such circumstance, the choice of regularization parameter needs to be guided by the physical understanding of the specific problem. Thus we devote this section to examine the effect of regularization parameter on the numerical solution for the three examples.

In the first place, we examine how the regularization parameter affects the numerical solution of inverting two superposed exponential relaxations. In the top panels of Fig. 4.2, we show the results using clean $F_s(t)$ data as input. Figure 4.2(a) shows the input $F_s(t)$ and two numerical solutions of the A-R relation using different regularization parameters. The solution presented in the previous section is plotted as filled circles, while a new numerical solution using a larger regularization parameter is plotted as empty circles. As we can see, using a larger regularization parameter leads to peak broadening. It still produces a reasonable numerical

solution resembling the two δ functions. In Fig. 4.2(b), we plot the least squares term $\chi_{lsq} = ||\mathbf{y} - \mathbf{Cx}||_2^2$ and the regularization term $\chi_{reg} = ||\mathbf{Rx}||_2^2$ as a function of regularization parameter λ (see Eqs. (3.10) and (3.16) for notations). As λ increases, an increasing penalty is enforced on the regularization term χ_{reg} and thus its value drops. On the contrary, χ_{lsq} increases with λ. We then show the L-curve for this example in Fig. 4.2(c). However, the curve does not show an "L" shape, which implies that the L-curve criterion is ill-defined in this case.

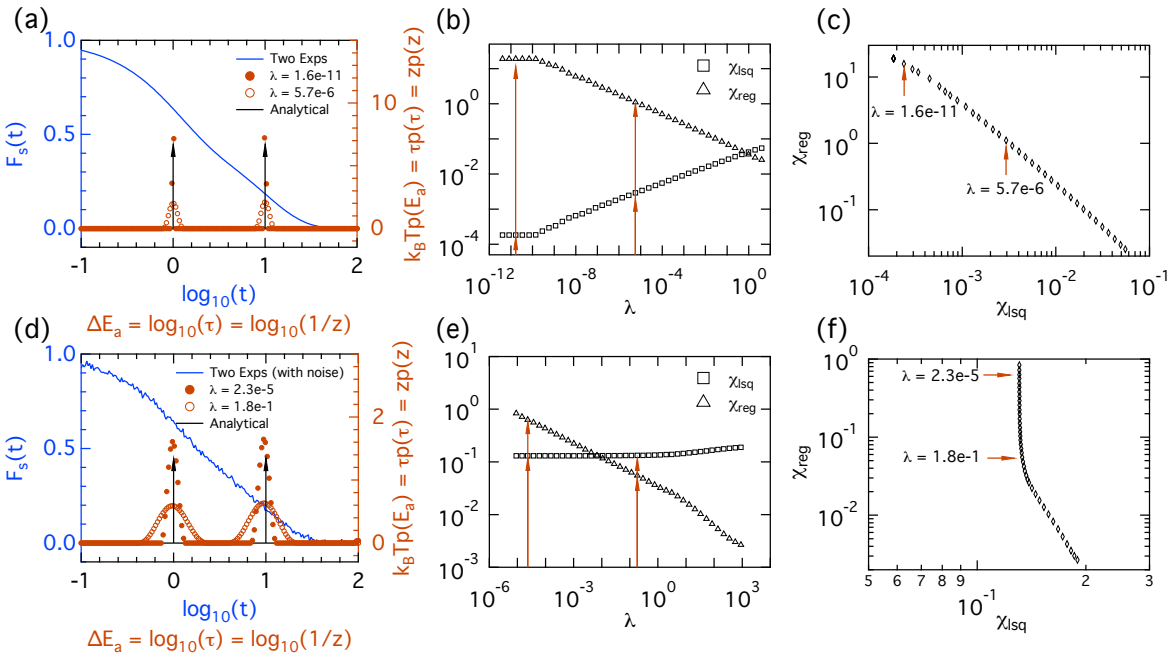

Figure 4.2: Effect of the regularization parameter λ on the numerical ILT solutions in the example of two superposed exponential decays. Two cases are shown: clean input data of $F_s(t)$ (top row), and noisy input (bottom row). In the noisy case, white Gaussian noises were added to the clean $F_s(t)$ data such that a signal-to-noise ratio of 35 dB was reached. The first column shows two numerical solutions of ILT given two different regularization parameters. The solution presented in the previous demonstration is shown using filled circles and the other solution is plotted using empty circles. Plots in the second column show the least squares term χ_{lsq} and the regularization term χ_{reg} as a function of regularization parameter λ. Specifically, $\chi_{lsq} = ||\mathbf{y} - \mathbf{Cx}||_2^2$ and $\chi_{reg} = ||\mathbf{Rx}||_2^2$ (see Eq. (3.10) and (3.16)). The positions of the two λ's used in the panel (a) are marked with arrows. The third column shows χ_{lsq} vs. χ_{reg} in the log-log plot, i.e. the "L-curve".

Besides inputting clean data, we examine another case which uses noisy $F_s(t)$ data as input. The noisy data possess considerable white Gaussian noise to the extent of signal-noise-ratio of 35 dB. Similar analyses are shown in the bottom row of Fig. 4.2. Due to the increased noise, a larger regularization parameter is needed to stabilize the problem. As is shown, the numerical method still works reliably to reconstruct the two singular δ functions from such noisy data. Unlike the first case, in Fig. 4.2(c) we observed a better

defined L-curve in this noisy case. Using the λ value determined from the corner of the L-curve produces a significant broadening of the peaks in the A-R relation. Thus for this special example (note that the δ function is numerically singular), we stick to a small regularization parameter $\lambda = 2.3e-5$ when presenting the final numerical result.

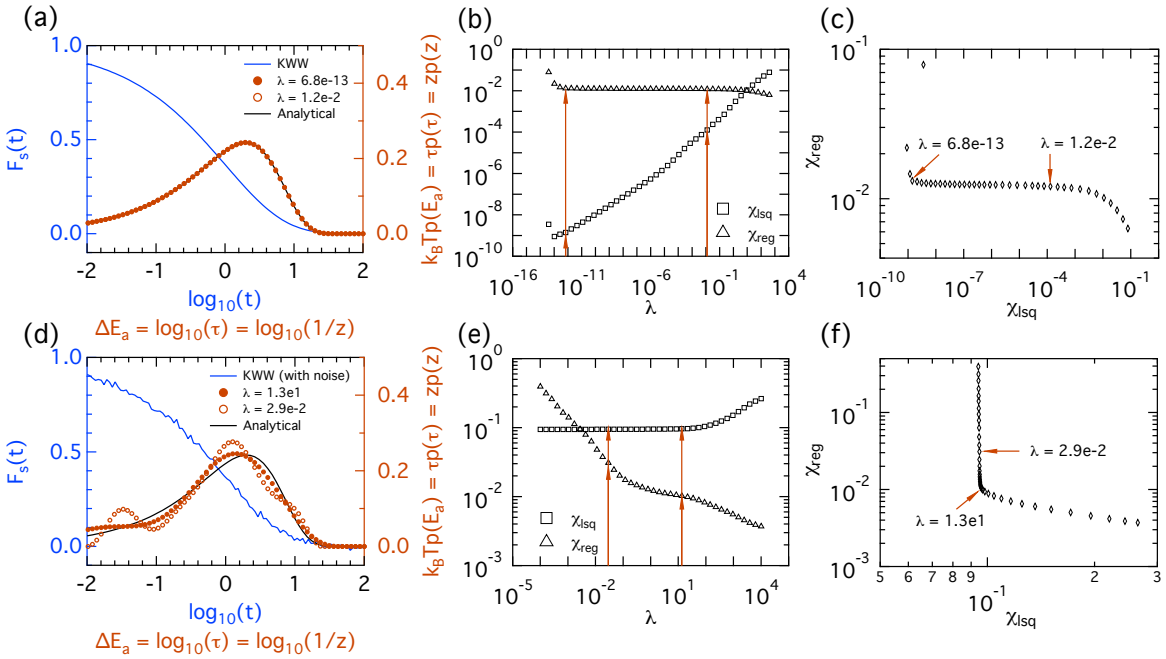

Figure 4.3: Effect of the regularization parameter λ on the numerical solutions in the example of stretched exponential (KWW) function. Two cases are shown: clean input data of $F_s(t)$ (top row), and noisy input (bottom row). In the noisy case, a signal-to-noise ratio of 35 dB was reached by adding white Gaussian noise to the clean $F(t)$ data. The first column shows two numerical solutions of ILT given two different regularization parameters. The solution presented in the previous demonstration is shown using filled circles and the other solution is plotted using empty circles. The second column shows the least squares term χ_{lsq} and the regularization term χ_{reg} as a function of regularization parameter. The third column shows the "L-curve", namely, χ_{lsq} vs. χ_{reg} in the log-log plot. In both cases, the curves show a pronounced "L" shape. Thus the λ corresponding to the corner of the L-curve was chosen to present the final solution in the previous demonstration.

Next, we move on to the second example, i.e., stretched exponential (KWW) relaxation. Again, we examine two test cases where clean data and noisy data were used as input. We show similar analyses as those in the last example in Fig. 4.3. In the case of clean input, Fig. 4.3(a) reveals that the numerical solution is largely independent of regularization parameter over a very wide range. Nevertheless, this is not true for noisy input. A large regularization parameter is necessary to help suppress unphysical oscillations. Moreover, both cases show well defined L-curves. Thus, when presenting the final result, we use the regularization parameter defined from the corner (the point of maximum curvature) of L-curve.

Finally, we examine the third example where the relaxation arises from a Gaussian AE-PDF defined by Eq. 4.10. The results are shown in Fig. 4.4. For both cases of clean input and noisy input, the numerical solution shows very little dependence on the regularization parameter over a very wide range. The L-curve criterion fails in the form case since an "L" shape was not observed in Fig. 4.4. However, for the later case, the L-curve is well defined and provides an optimal regularization parameter.

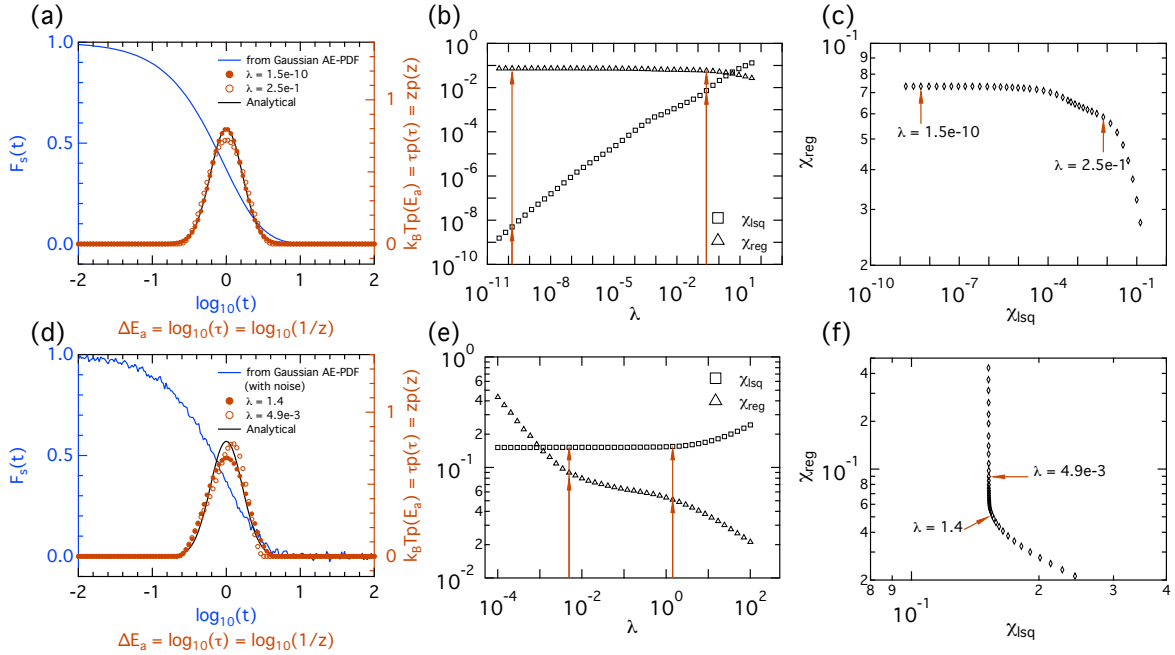

Figure 4.4: Effect of regularization parameter λ on the numerical solutions of ILT in the example of Gaussian AE-PDF. The $F(t)$ data were obtained by integrating the Gaussian AE-PDF's. Two cases are shown: clean input data of $F(t)$ (top row), and noisy input (bottom row). In the noisy case, white Gaussian noise was added to the clean $F(t)$ data, reaching a signal-to-noise ratio 35 dB. The first column shows two numerical solutions of ILT given two different regularization parameters. The solution presented in the previous demonstration is shown using filled circles and the other solution is plotted using empty circles. The second column shows the least squares term χ_{lsq} and the regularization term χ_{reg} as a function of regularization parameter λ. The third column shows the "L-curve" χ_{lsq} vs. χ_{reg} in log-log plot. An "L" shape was observed in the second case, but not in the first case.

Chapter 5

Application of Relaxation Mode Analysis to a Kob-Andersen Liquid

5.1 Simulation Details

In this chapter, we applied RMA to study the relaxation behaviors of a widely studied binary Lennard-Jones mixture [87, 88] (commonly known as Kob-Andersen liquid) using molecular dynamics (MD) simulations. The simulation system consisted of 1500 particles of two species, i.e A (80%) and B (20%), in a periodic cubic box. Particles interacted with each other via the Lennard-Jones potential

$$V_{\alpha\beta}(r) = 4\epsilon_{\alpha\beta}\left[\left(\frac{\sigma_{\alpha\beta}}{r}\right)^{12} - \left(\frac{\sigma_{\alpha\beta}}{r}\right)^{6}\right], \quad \alpha, \beta \in A, B \tag{5.1}$$

where in reduced units $\epsilon_{AA} = 1.0,\ \sigma_{AA} = 1.0,\ \epsilon_{BB} = 0.5,\ \sigma_{BB} = 0.88,\ \epsilon_{AB} = 1.5,\ \sigma_{AB} = 0.8$. Interactions beyond cut-off distance $2.5\sigma_{AA}$ were shifted and truncated. Periodic boundary condition was applied in three dimensions. To utilize GROMACS, these reduced numbers were converted to real physical values in terms of reference values for argon. A unit length is 0.34 nm and unit energy is $k_B T_{ref}$ with $T_{ref} = 120$ K. Both species of particles have the same mass 39.948 u. A typical snapshot of the simulated system is shown in Fig. (5.1).

Below we outline the simulation procedures following Ref. [87]. The system was first equilibrated at high temperature 480 K (or 4.0 in reduced unit). It was then cooled down step by step to 9 lower temperatures, i.e. 360 K, 240 K, 180 K, 120 K, 96 K, 72 K, 66 K, 60 K, during a period of time length larger than the relaxation time of system at the targeted temperature. Afterwards, the system kept contacting with a thermostat at the target temperature for a period of time comparable to cooling time. This was followed by a short NVE simulation run to check the equilibrium. If no significant drifts in ensemble averaged quantities, such as temperature and potential energy, were observed, we considered the system in equilibrium and thereby production runs using NVT ensemble were carried out to collect simulation trajectories for post-analysis.

In the following sections, we apply RMA to study the relaxations in the simulated Kob-Andersen liquid, focusing on analyzing the dynamical properties of the primary particle species A. Two key aspects, the

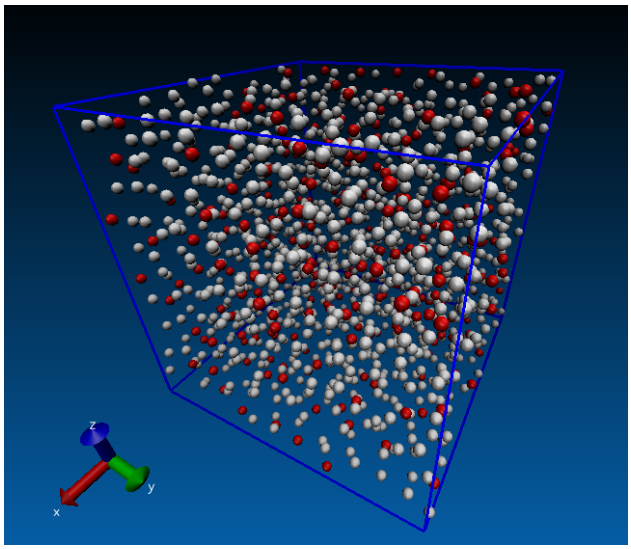

Figure 5.1: A snapshot of the Kob-Andersen liquid from MD simulations. The primary particle species A (80%) is colored in white, and the other species B (20%) in red.

temperature dependence and wavevector transfer dependence, are examined. Similar to the demonstrations in last chapter, we use the A-R relation to show the three important distribution functions, namely, AE-PDF, RT-PDF, and RR-PDF. In particular, we focus on the AE-PDF and interpret figures from the perspective of energy landscape.

5.2 Temperature Dependence: Dynamical Decoupling

First, we examine the temperature effect on the relaxation of this Kob-Andersen liquid using RMA. The relaxation behaviors at three temperatures are shown in Figure. 5.2, with wavevector transfer k chosen near the structure factor peak. At the highest temperature (Fig. 5.2(a)), the intermediate scattering function shows an exponential-like decay and a sharp peak appears in the AE-PDF. As the temperature decreases, the long time tail of the intermediate scattering function becomes more and more stretched, eventually forming a plateau in the intermediate time range. Accordingly, the AE-PDF evolves from a narrow peak at the high temperature, to a overlapping bimodal shape at the intermediate temperature, and to a multimodal distribution at the lowest temperature.

From the perspective of energy landscape, these obeseved varitions suggest the topography of free energy landscape strongly depends on the temperature. At high temperatures, the overwhelming thermal energy dominates over the energy differences among different configurations. The sampling of different configurations is almost equally probable. Fig. 5.2(a) shows the AE-PDF is centered at a small activation energy,

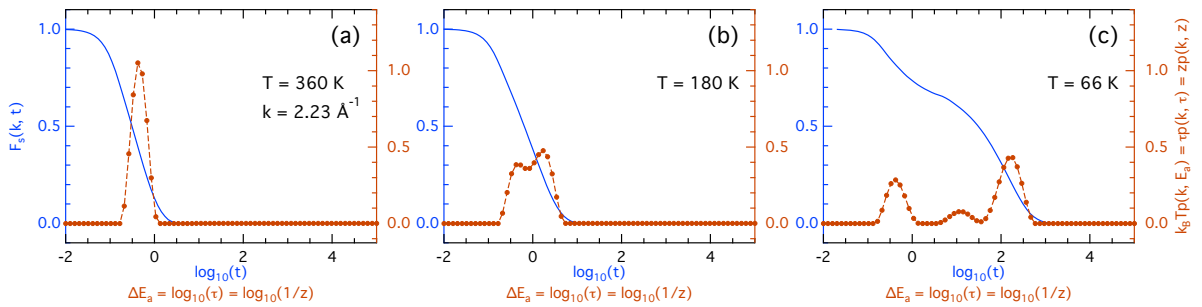

Figure 5.2: Intermediate scattering functions (blue curves) of particle species A and the resulting A-R relations (orange curves) extracted by RMA at three temperatures. The units of variables are as follows: ΔE_a [$\ln(10) k_B T$], τ [ps], and z [ps^{-1}]. ΔE_a is related to the absolute activation energy E_a by $\Delta E_a = E_a - k_B T \ln z_0$. The wavevector transfer $k = 2.23$ Å^{-1} is chosen near the location of the first peak of static structure factor. As temperature decreases, the A-R relation varies from a narrow unimodal shape, to a overlapping bimodal shape, and eventually to a distribution with multiple well-separated peaks. This peak separation suggests different origins of the relaxations. The regularization parameter determined from the L-curve criterion was $\lambda = 4.3e - 3$. This value was used in all the analyses presented in this chapter.

suggesting the existence of a large population of shallow energy minima. As the temperature decreases, the free energy landscape deforms towards the shape with increasingly deep minima. The configurations associated with these deep minima are more favored compared to others. Hence, at low temperatures, the interplay between the large population of shallow minima and the increased depth of deep minima gives rise to the multimodal distribution of activation barriers.

Moreover, the extracted AE-PDF also implies the manners in which different relaxation modes depend on the temperature in the real space. Low activation barriers lead to fast relaxations, while high activation barriers cause slow relaxations due the time spent in overcoming the barriers. The fast relaxation mode has a relaxation time scale almost independent of temperature. A common interpretation relates this behavior to short-time relaxation inside a cage formed by nearest neighbor particles. This in-cage relaxation mainly depend on static packing geometry and thus has little temperature dependence. In contrast, the time scale of slow relaxation mode increases substantially as the temperature decreases. This behavior is attributed to diffusional relaxations outside cages, which largely rely on the available thermal energy.

The origins of distinct relaxation modes can be identified by separating them at different spatial length scales. As the wavevector transfer k is inverse proportional to the length scale at which the system is probed, adjusting the k value enables us identify the mechanisms governing different relaxation modes. In Fig. 5.3 we show the temperature dependence of the intermediate scattering functions and the resulting AE-PDF's extracted at three k values. The probing length scale corresponding to the structure factor peak ($k = 2.23$ Å^{-1}) is close to the cage sizes formed by the nearest neighbors surrounding particles. Similar to

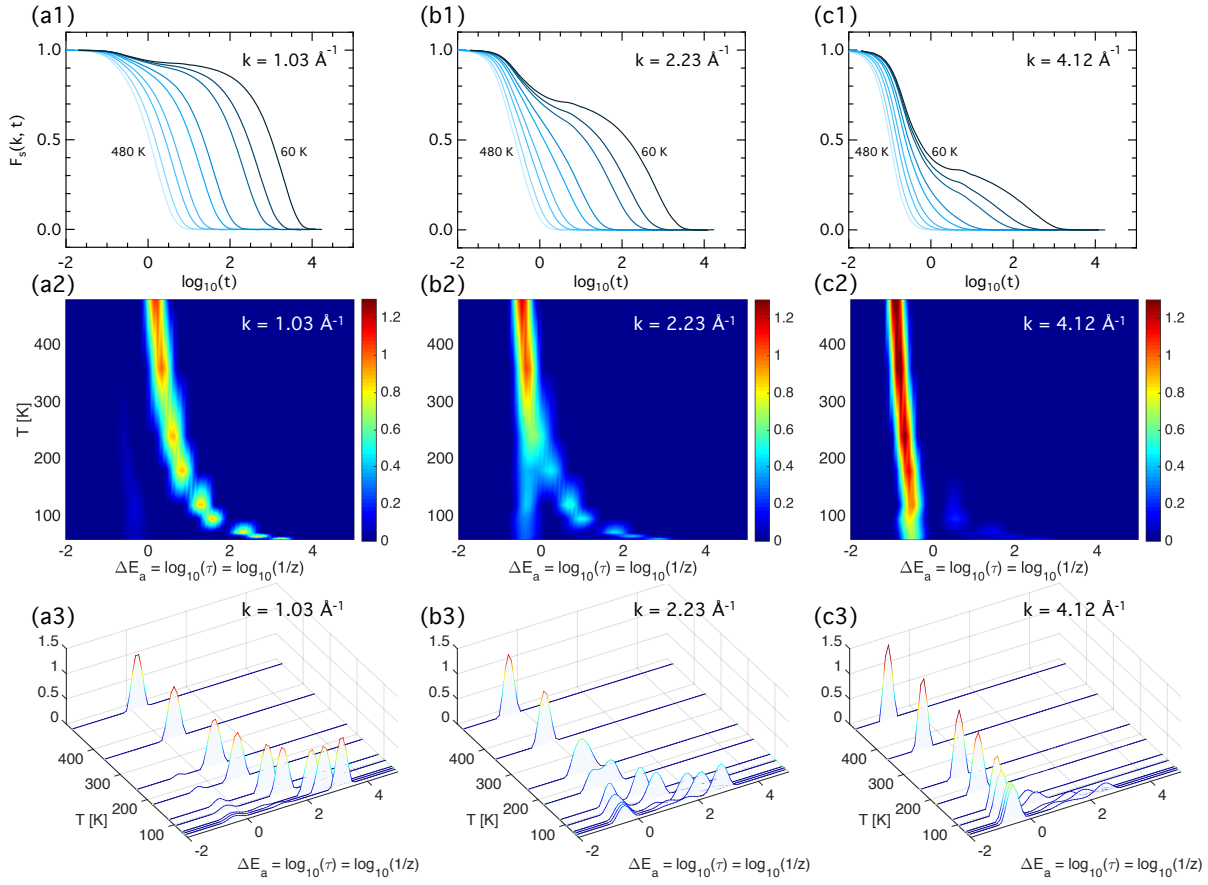

Figure 5.3: Temperature dependence of relaxations of particle species A examined by RMA at three values of the wavevector transfer: (a) 1.03 Å^{-1}, (b) 2.23 Å^{-1} (near the structure factor peak), (c) 4.12 Å^{-1}. Different k values imply different spatial resolutions at which the system is probed. The top row shows the temperature dependence of intermediate scattering functions. In the second row, the temperature-dependent AE-PDF's are shown as pseudo-color images, in which the colors indicate the intensities of the A-R relation $k_B T p(\mathbf{k}, E_a) = \tau p(\mathbf{k}, \tau) = z p(\mathbf{k}, z)$. The bottom row shows the shapes of the extracted AE-PDF's in a three-dimensional view. In all cases, the regularization parameter used for numerical ILT is $\lambda = 4.3e - 3$.

Fig. 5.2, the extracted AE-PDF's shown in Fig. 5.3(b2) manifest the decoupling of slow and fast relaxation modes with decreasing temperature. The mechanism behind each relaxation can be understood from the AE-PDF's extracted at other length scales. At a larger length scale ($k = 1.03$ Å^{-1}), the fast peak of the extracted AE-PDF (Fig. 5.3(a2)) fades, while the slow peak stays prominent. However, at a smaller length scale ($k = 4.12$ Å^{-1}), the opposite behavior was observed. These observations further support that the temperature-independent fast relaxation involves short-time motions inside cages, and the temperature-dependent slow relaxation relate to diffusion out of cages.

From Fig. 5.3, we are able to calculate the most probable relaxation times and activation energies associated with different relaxation modes as a function of temperature. Figure 5.4 shows the results. The first row shows the most probable relaxation times as a function of temperature at three k values. For

comparision, we also plot the α-relaxation time (the slowest relaxation time) defined from $1/e$ cut of $F_s(k,t)$. In addition, in Fig. 5.4(b1), these timescales are compared to another two characteristic α-relaxation times defined by other approaches, i.e. the peak location of non-Gaussian parameter $\alpha_2(t)$ [15] and the peak location of four-point susceptibility $\chi_4(t)$ [16, 14]. Over the k range where the slow relaxation peak in the A-R relaxation is clearly defined, these α-relaxation times agree with the most probable relaxation time of the slow relaxation mode identified from the A-R relation. More importantly, from Fig. 5.4(b1), we identified the temperature where the fast relaxation and slow relaxation decouples as $T_o = 180 \sim 240K$ (or in the reduced unit $T_o = 1.5 \sim 2.0$). This dynamic decoupling temperature coincides with the temperature below which the peaks of $\alpha_2(t)$ and $\chi_4(t)$ both start to grow abruptly. This coincidence indicates the onset of dynamic heterogeneity, which will be discussed in section 5.4.

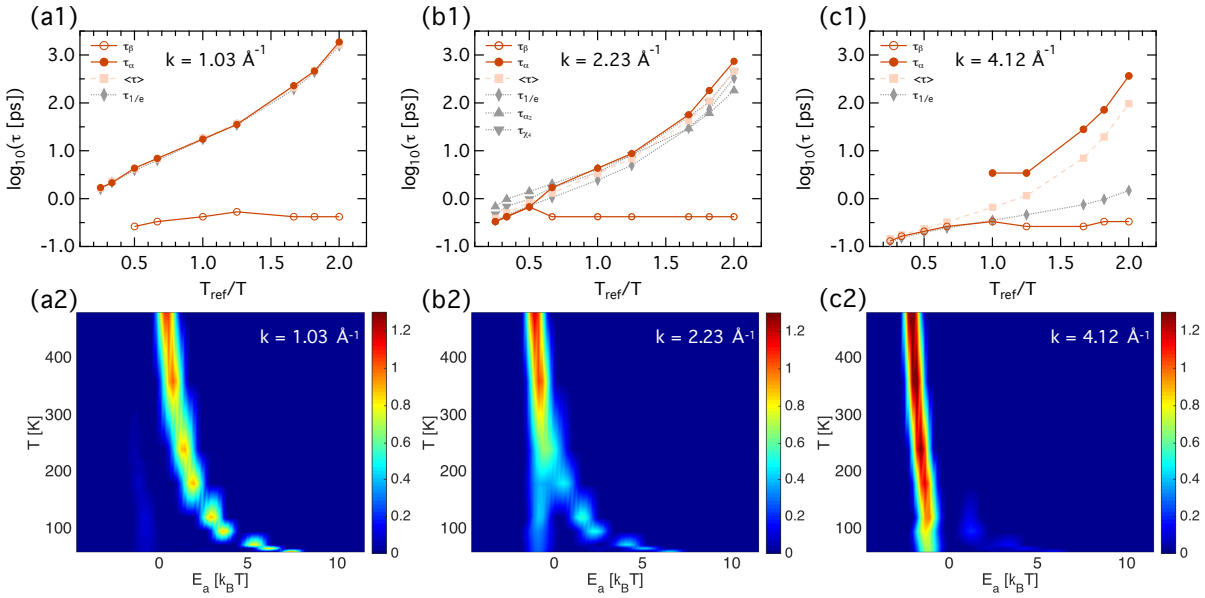

Figure 5.4: Temperature dependence of the most probable relaxation times and activation energies extracted from Fig. 5.3. The top row shows the temperature dependence of the most probable relaxation times of relaxation processes indicated by the peak locations of the A-R relations shown in Fig. 5.3. Here $T_{ref} = 120$ K. Panel (b1) also shows the relaxation times defined by other approaches, for example, $1/e$ cut of intermediate scattering function, the peak location of non-Gaussian parameter $\alpha_2(t)$, and the peak location of four-point susceptibility $\chi_4(t)$. (see section 5.4). The second row shows the AE-PDF's versus the absolute activation energy E_a expressed in the unit of k_BT. ΔE_a is related to the absolute activation energy E_a by $\Delta E_a = E_a - k_BT \ln z_0$. The conversion from ΔE_a to E_a was done by extrapolating the relaxation times to infinite temperature at small k value and thereby determining $z_0 = 1/\tau_0 = 1$ ps^{-1}.

In the second row of Fig. 5.4, the temperature-dependent AE-PDF was plotted versus the absolute activation energy E_a in terms of unit k_BT. The conversion from ΔE_a (in the unit of $\ln(10)k_BT$) in Fig. 5.3 to E_a ($= \Delta E_a + k_BT \ln z_0$) in Fig. 5.4 is determined up to a shift specified by the prefactor z_0 (see Eq. 2.19). We estimated this z_0 value by extrapolating the relaxation time to infinite temperature at small k values,

which gave $z_0 = 1/\tau_0 = 1$ ps^{-1}. Ideally, the absolute activation energy E_a should be a nonnegative quantity. The appearance of negative E_a in Fig. 5.4 is due to the uncertainty of determining z_0 (or τ_0) in the conversion from ΔE_a to E_a.

5.3 Wavevector Transfer Dependence: Energy Landscape Coarsening

In this section, we consider the wavevector transfer k dependence of the observed relaxational dynamics of A particles at fixed temperatures. In essence, the inverse of k value defines the length scale at which the material system is probed. Adjusting k values can be utilized to identify the governing motions at different length scales. Figure 5.5 shows the RMA results as a function of k at three temperatures. Given the intermediate scattering functions at the first row as input, the extracted AE-PDF's are shown as pseudo-color images at the second row and waterfall plots at the bottom. In the second row, the dashed lines indicate the hydrodynamic limits ($k \to 0$) of α-relaxation times $\tau_{\text{hydro}} = 1/D_0(T)k^2$, where $D_0(T)$ is the temperature-dependent self diffusion coefficient. According to Fig. 5.5(a2), single relaxation trace dominates across different length scales at this high temperature case. The relaxation time increases with a decreasing k and shows a good agreement with the hydrodynamic limit. This agreement implies the diffusive characteristics of relaxations at high temperatures. As the temperature lowers, multiple relaxation peaks appear and follow different transition patterns as k varies. On the one hand, the fast relaxation peak dominates in an almost constant timescale at the large k range and gradually fades away as k decreases. This trend supports that the fast relaxation is attributed to inside-cage relaxations. On the other hand, the slow relaxation peak migrates to larger relaxation times with decreasing k, eventually following the hydrodynamics limit at small k. This agreement indicates that diffusive motions are mainly responsible for the slow relaxation.

Next, we show in Fig. 5.6 the k dependence of the most probable relaxation times and activation energies extracted from Fig. 5.5. The most probable relaxation times of different relaxations are compared to the relaxation times from other definitions, e.g. the first moment of RT-PDF, $1/e$ cut of $F_s(k,t)$, and the hydrodynamic limit. At high temperatures all the curves collapse, while at low temperatures obvious discrepancies exist. In the second row of Fig. 5.6, we show the AE-PDF versus the absolute activation energy E_a in the unit of k_BT. Note that the k axes are plotted on logscale. In such plots, the slow relaxation traces at small k regime becomes straight lines because of their agreements with the hydrodynamic limits.

As manifested in Fig. 5.5 and 5.6, the k dependence of the AE-PDF suggests that different relaxation modes dominates at different length scales. From the viewpoint of energy landscape, these observations

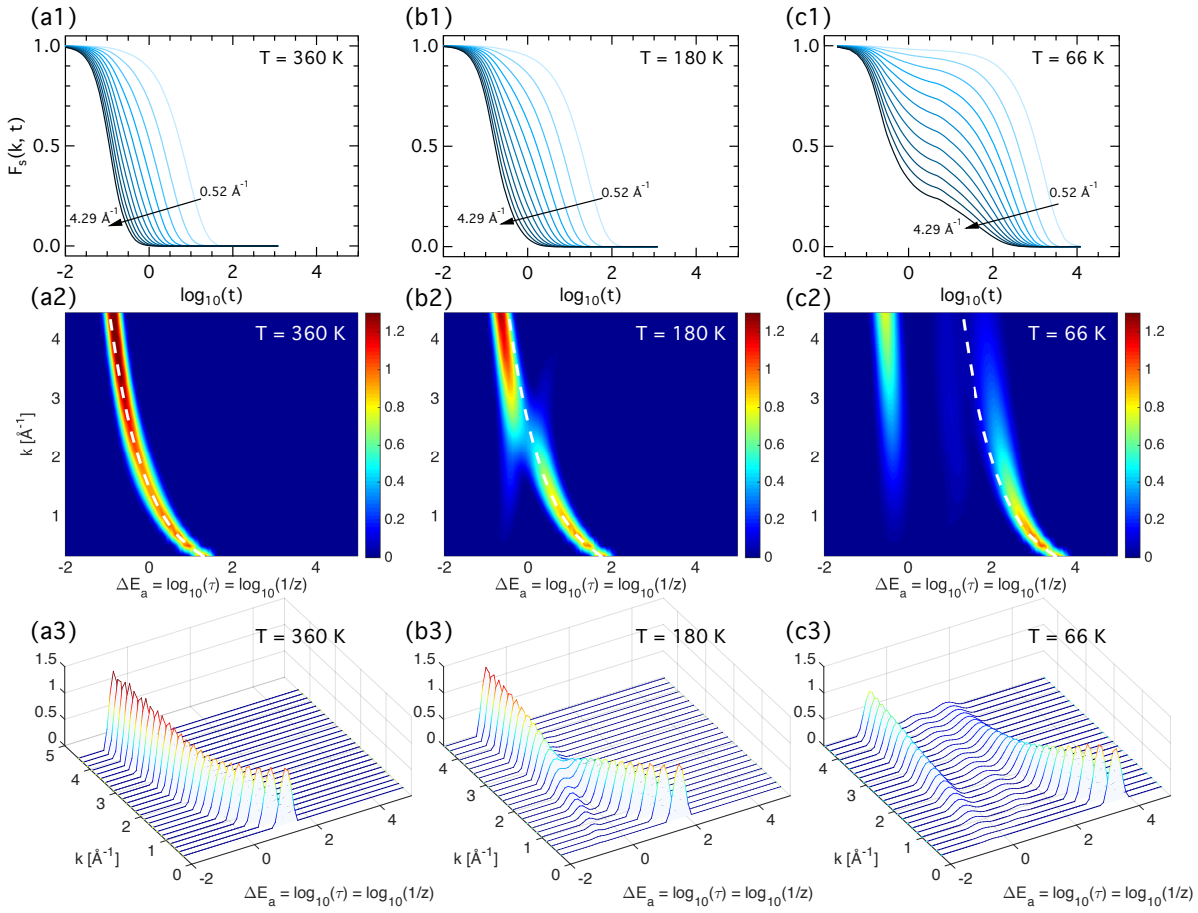

Figure 5.5: Wavevector transfer dependence of teh relaxations of particle species A examined by RMA at three temperatures: (a) 360 K, (b) 180 K, (c) 66 K. The top row shows the k dependence of intermediate scattering functions. For clarity, not all curves of computed k's are shown explicitly. In the second row, the pseudo-color images show the k dependence of the extracted A-R relations $k_BTp(\mathbf{k}, E_a) = \tau p(\mathbf{k}, \tau) = zp(\mathbf{k}, z)$, with intensities indicated by colors. On top of each pseudo-color plot, the hydrodynamic limit ($k \to 0$) of α-relaxation, $\tau_\alpha = 1/(D_0(T)k^2)$, is also plotted in the dashed line. The temperature-dependent diffusion coefficients $D_0(T)$ were obtained by linearly fitting the long time tail of mean square displacement (see Fig. 5.8(a)). The third row shows a three-dimensional view of the same A-R relations as in the second row. The regularization parameter used for numerical ILT is $\lambda = 4.3e-3$.

reveal an interesting coarsening effect of the energy landscape (see Fig. 5.7). Using a large k value, we are able to probe fine topographic features on the energy landscape. As a consequence, the extracted AE-PDF is dominated by small activation barriers separating nearby shallow basins. In contrast, probing the potential energy landscape with a small k ignores the detailed features but focuses on the large-scale topographic structures on the energy landscape. Therefore, high activation barriers are highlighted in the extracted AE-PDF.

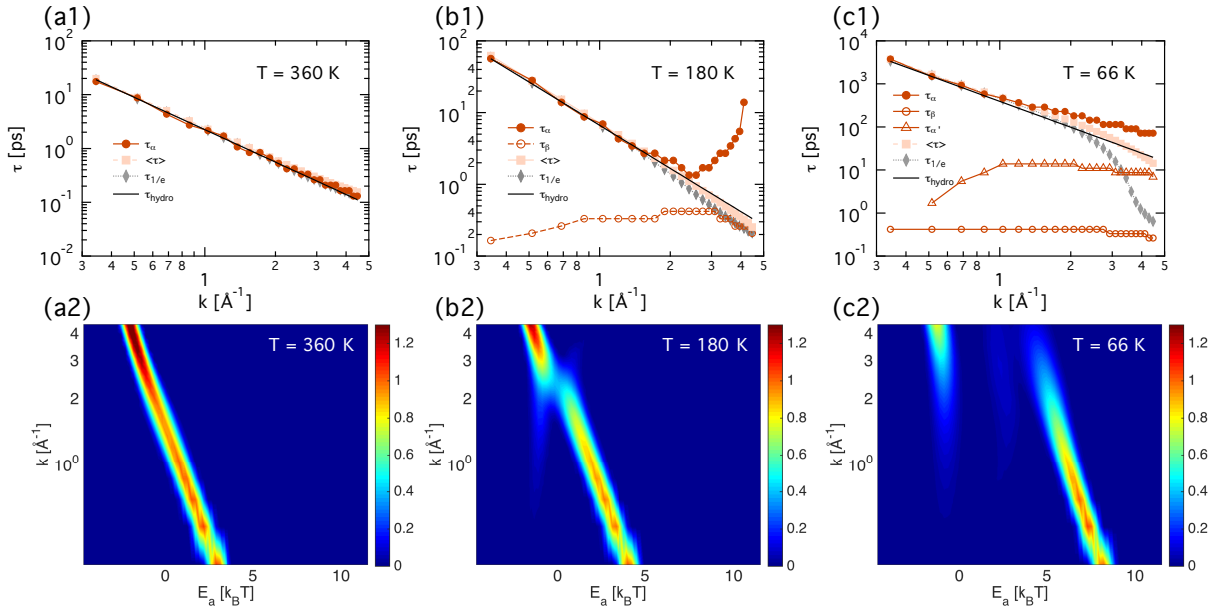

Figure 5.6: Wavevector transfer dependence of the most probable relaxation times and activation energies of particle species A extracted from Fig. 5.5. The first row shows the most probable relaxation times as a function of k for different relaxation processes. Various relaxation processes exist at low temperatures. The second row shows the k dependence of the A-R relation $k_BTp(\mathbf{k}, E_a) = \tau p(\mathbf{k}, \tau) = zp(\mathbf{k}, z)$. Note that in the plots the k axes are plotted on log scale, and the absolute activation energy E_a has the unit of k_BT. The conversion from ΔE_a $(= E_a - k_BT \ln z_0)$ to E_a was done by extrapolating the relaxation times to infinite temperature at small k value and thereby determining $z_0 = 1/\tau_0 = 1$ ps^{-1}.

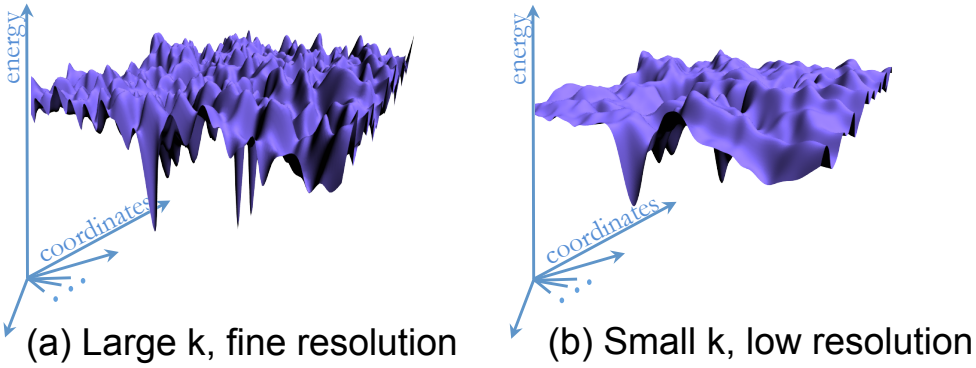

Figure 5.7: Illustration of energy landscape coarsening. (a) A large k means high-resolution measurement and the sampled energy landscape shows fine structures. (b) A small k neglects detailed structures but focuses on detecting the large-scale structures of the energy landscape.

5.4 Dynamic heterogeneity

As mentioned in section 1.1, dynamic heterogeneity refers to spatial heterogeneous dynamics correlated between distinct relaxing domains [10, 11, 12, 13]. The emergence of dynamic heterogeneity with decreasing temperature is a very improtant dynamical signature in supercooled liquids approaching the glass transition. At high temperatures, particles can move independently and homogeneous dynamics dominates the system. As the temperature lowers and dynamics becomes more and more sluggish, structural rearrangements occur in a cooperative manner. Neighboring particles with similar mobilities form local clusters to facilitate movements. The correlation length of such spatiotemporal correlations grows substantially towards the glass transition[12, 14].

In Fig. 5.8, we characterize the dynamic heterogeneity using three important dynamic quantities, i.e. the mean square displacement (MSD), non-Gaussian parameter [15], and four-point correlation function [14, 16]. First, Fig. 5.8(a) shows the temperature dependence of mean squares displacement

$$\langle \Delta \mathbf{r}^2(t) \rangle \equiv \langle |\mathbf{r}_j(t) - \mathbf{r}_j(0)|^2 \rangle, \tag{5.2}$$

where $\mathbf{r}_j(t)$ is atomic position at time t and $\langle \cdots \rangle$ means ensemble average. As we can see, the MSD's display multi-step growth at low temperatures. The macroscopic diffusion coefficient can then be extracted by fitting the long time tail of MSD with the Einstein relation $\langle \Delta \mathbf{r}^2(t) \rangle = 6Dt$. Equiped with the diffusion coefficient and relaxation time, we can examine the validity of the Stokes-Einstein relation, which connects the diffusion coefficient D, bulk viscosity η, and temperature T via $D \propto T/\eta$ [89]. As viscosity is inversely proportional to the α-relaxation time, the Stoke-Einstein relation is also commonly written as $D \propto T/\tau_\alpha$ [89]. This relation is typically valid at high temperatures but breaks down due to the emergence of dynamic heterogeneity in the supercooled regime. Thus we plot $D\tau_\alpha/T$ vs. T in Fig. 1.1(d). The deviation of $D\tau_\alpha/T$ from a constant signifies the development of dynamic heterogeneity.

Moreover, we show in Fig. 5.8(b) the non-Gaussian parameter [15]

$$\alpha_2(t) = \frac{3\langle |\mathbf{r}_j(t) - \mathbf{r}_j(0)|^4 \rangle}{5\langle |\mathbf{r}_j(t) - \mathbf{r}_j(0)|^2 \rangle^2} - 1, \tag{5.3}$$

and in Fig. 5.8(c) a four-point correlation function [14, 16]

$$\chi_4(t) = \frac{V}{T} \langle Q_s^2(t) \rangle - \langle Q_s(t) \rangle^2, \tag{5.4}$$

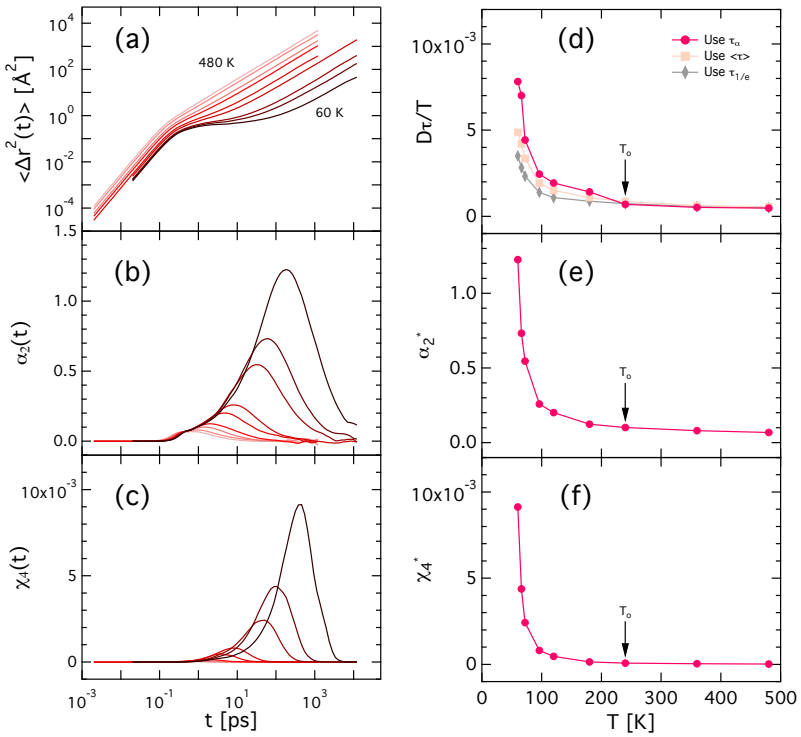

Figure 5.8: Dynamic heterogeneity illustrated by the temperature dependence of (a) mean square displacement, (b) non-Gaussian parameter $\alpha_2(t)$, and (c) four-point susceptibility $\chi_4(t)$. (d) The breakdown of Stokes-Einstein relation at low temperatures. (e)(f) Abrupt growth of $\alpha_2(t)$ peak and $\chi_4(t)$ peak at low temperatures. The temperature at which the bifurcation of α relaxation and β relaxation first appears in the AE-PDF (see Fig. 5.3(b1) and 5.3(b2)) is marked as T_o in the plots (d)(e)(f).

where

$$Q_s(t) = \frac{1}{N}\sum_{j=1}^{N} w\left(|\mathbf{r}_j(t) - \mathbf{r}_j(0)|\right) \tag{5.5}$$

The overlapping function $w\left(|\mathbf{r}_j(t) - \mathbf{r}_j(0)|\right)$ is unity inside a region of size a and zero outside, where the value of a (1 Å) was taken slightly larger than the square root of the plateau value of MSD [14]. In Eq. (5.4), V is the system volume and T is the temperature. Both $\alpha_2(t)$ and $\chi_4(t)$ show a unimodal shape with the peak location designating a characteristic α-relaxation timescale. As temperature decreases, both peaks shift to larger timescales. The abrupt growth of the peak intensities signals the development of dynamic heterogeneity (Fig. 5.8(e) and 5.8(f)).

These results can be compared to those from RMA presented in last sections. The capability to decouple distinct relaxation modes at different length and time scales makes RMA a promising tool to study dynamic heterogeneity. On the one hand, at a fixed length scale as indicated in Fig. 5.4(b1) and 5.4(b2), the prevalence of single relaxation mode implies homogeneous dynamics at high temperature. As the system cools down,

the emergence of extra relaxation modes signifies the development of dynamic heterogeneity. Recall that the decoupling temperature for slow relaxation and fast relaxation was identified at $T_o = 180 \sim 240$ K. In the right column of Fig. 1.1, this decoupling temperature is shown to coincide with the temperature below which the Stokes-Einstein relation breaks down, and both peaks of $\alpha_2(t)$ and $\chi_4(t)$ grow abruptly.

Chapter 6

Conclusions and Future Work

6.1 Conclusion

The energy landscape is an important framework to help understand slow processes in many physical systems. In particular, it has been widely applied to study the dynamics of supercooled liquids and glass transition. Despite numerous simulation studies, however, the challenge still remains how to quantify the energy landscape statistics from experiments.

To address this challenge, we proposed a relaxation mode analysis (RMA) for liquids in this thesis by drawing analogy to the normal mode analysis for solids. Based on the experimentally measurable two-point density-density correlation function (intermediate scattering function), our method projects the complicated motions of liquids into a distribution of elementary relaxation modes in the relaxation rate domain. An activation-relaxation relation was then derived to connect three important distribution functions, namely, relaxation rate probability distribution function (RR-PDF), relaxation time probability distribution function (RT-PDF), and activation energy probability distribution function (AE-PDF). In this derivation, the relaxation rate is mapped to the activation energy barrier by considering relaxations occur by overcoming activation energy barriers on the energy landscape. It is this activation-relaxation relation that provides a possibility to extract the important statistics of activation barriers from experimental data.

As demonstrations, we used RMA to analyze three common relaxation functions, i.e. exponential decay, stretched exponential decay, and relaxation function corresponding to a Gaussian-distributed AE-PDF. In addition, RMA was applied to study relaxational dynamics of a Kob-Andersen liquid with the help of molecular dynamics simulations. Two key factors, the temperature and wavevector transfer k, were examined. On the one hand, studying the temperature dependence revealed that single relaxation mode dominated the system at high temperatures and additional relaxation modes emerged as the temperature gradually drops. This behavior indicated the emergence of dynamic heterogeneity as system became supercooled. On the other hand, adjusting the wavevector transfer k revealed the dominant length scales of different relaxation modes. The slow relaxations were associated with crossing high activation barriers between large basins,

while the fast relaxations were related to transitions between nearby shallows basin embeded in the large ones. The variations of AR-PDF with k reveals an interesting coarsening effect of the energy landscape.

Furthermore, RMA provides a model-independent approach to analyze experimental data, for example, from quasi-elastic neutron scattering measurements. From the measured intermediate scattering functions, RMA is able to extract relaxtion modes at different length and time scales without adopting empirical fitting functions.

6.2 Future Work

The framework of RMA can be improved in the future from several persepctives, for example, applying RMA to complex systems, extending the theoretical framework of RMA, and improving numerical methods for inverse Laplace transform.

- Applying RMA to complex materials:

  In this thesis, we demonstrated the capabilities of RMA by studying empirical examples and a Kob-Andersen liquid simulated by molecular dynamics simulations. An important follow-up is applying this approach to analyze experimental measurments. It would be interesting to see the underlying distributions of relaxation modes and activation energy barriers for different materials. Moreover, although RMA was originally developed for liquids, its framework can be applied to study more complex systems that exhibit relaxational dynamics. In particular, we are interested in applying RMA to study protein folding, a longstanding hot topic in the field of soft matter. Since a protein system has complicated compositions, it remains challenging to analyze the protein dynamics from neutron scattering measurements. Thus, studying this problem using RMA may help examine the applicability of RMA.

- Extending the theoretical framework of RMA:

  RMA builds upon the presumption that diffusion is the underlying elementary motion in liquids. To describe liquid dynamics, the intermediate scattering function is formulated as a linear superposition of elementary relaxation modes represented by exponential decays. Although this framework has its merit to analyze relaxation dynamics in many problems as we already demonstrated, some improvements can be done to extend its capability. For example, at very short time, the intermediate scattering function of liquids is a Gaussian [47] which decays faster than exponential decay and can not be decomposed as a linear summation of exponential decays. The current version of RMA hasn't included this feature. Therefore, in the future work, we would like to extend RMA to capture this short-time Gaussian

relaxation.

On top of that, liquids could exhibit solid-like excitations under extreme conditions such as low temperature and high pressure. For example, vibrational motions may introduce oscillatory features in the decay curve of the intermediate scattering function. To account for these features, it is compelling to unify the frameworks of relaxation mode analysis and normal mode analysis. The former quantifies the liquid-like diffusions and the later captures the solid-like excitations.

- Improving numerical methods for inverse Laplace transform:

  We have shown several numerical methods for inverse Laplace transform in Chapter 3. Despite the validity of the numerical method we adopted (see Chapter 4), we can still improve its performance in some aspects. For example, besides the common reguarizors introduced in section 3.3, new regularization functionals may be designed to penalize undesired features in the solution more efficiently. Also, choosing an appropriate value for regularization paramter plays an important role in the regularization method. Nevertheless, the exisitng strategies for choosing an optimal regularization parameter work case by case. A universal strategy to effectively determine the regularization parameter remains to be developed.

Appendix A

The generalized k-dependent diffusion coefficient

In section 2.1, a diffusion equation of self density-density correlation function $G_s(\mathbf{r},t)$ (Eq. 2.6) in real space gives rise to a first order differential equation of the self intermediate scattering function $F_s(\mathbf{k},t)$ (Eq. 2.7). We then generalized the k-independent macroscopic diffusion coefficient D_l to a k-dependent quantity $D_l(\mathbf{k})$ such that the deviation of relaxation rate $z(\mathbf{k})$ from k^2 dependence at finite k values can be accounted. The implications of this generalization are discussed below.

Using inverse Fourier transform, the generalized Eq. (2.8) in turn yields a generalized form of diffusion diffusion in real space

$$\partial_t G_s(\mathbf{r},t) = D_l(\mathbf{r}) \otimes \nabla^2 G_s(\mathbf{r},t) = \int d\mathbf{r}' D_l(\mathbf{r}-\mathbf{r}')\nabla^2 G_s(\mathbf{r}',t), \tag{A.1}$$

where $\otimes$ is the convolution notation and $D_l(\mathbf{r})$ is a spatially dependent diffusion coefficient. This generalization extends the ability of RMA to account for non-Einstein diffusion. Unlike a simple diffusion (Eq. (2.7)) where the mean square displacement follows Einstein relation

$$\langle \Delta\mathbf{r}^2(t)\rangle \equiv \langle |\mathbf{r}_j(t) - \mathbf{r}_j(0)|^2 \rangle = 6D_0 t, \tag{A.2}$$

this generalized diffusion Eq. (A.1) defines a mean square displacement by

$$\begin{aligned} \frac{d\langle r^2(t)\rangle}{dt} &= \frac{d}{dt}\int d\mathbf{r}\ r^2 G_s(\mathbf{r},t) \\ &= \int d\mathbf{r}\ r^2 \partial_t G_s(\mathbf{r},t) \\ &= \int d\mathbf{r}\ r^2 \left[D_l(\mathbf{r}) \otimes \nabla^2 G_s(\mathbf{r},t)\right]. \end{aligned} \tag{A.3}$$

At small k, the k-dependent diffusion coefficient reduces to the macroscopic diffusion coefficient

$$D_0 = \lim_{k\to 0} D_l(\mathbf{k}) = \lim_{k\to 0} \frac{z_l(\mathbf{k})}{k^2} = \lim_{k\to 0} \frac{1}{\tau_l(\mathbf{k})k^2} \tag{A.4}$$

which is the quantity commonly measured from experiments. In this limit, Eq. A.1 reduces back to a simple diffusion equation, and accordingly the Einstein relation is obeyed.

Appendix B

The CONTIN Algorithm

Once the Laplace inversion is set up as a regularized nonnegative least squares problem (RNNLS)

$$\chi^2 = ||\mathbf{y} - \mathbf{C}\mathbf{x}||_2^2 + \alpha^2||\mathbf{R}\mathbf{x}||_2^2 = \text{minimum} \tag{B.1}$$

under nonnegative constraint $x \geq 0$, the CONTIN algorithm [59] can be applied to solve for a unique solution. This algorithm converts a RNNLS problem into a least distance programming (LDP) problem, which can be further solved efficiently.

(1) *Converting RNNLS to LDP*: The conversion is achieved by a sequence of singular value decompositions and variable replacements. First, the singular value decomposition of $N_{reg} \times N_x$ matrix $\mathbf{R}$ is computed

$$\mathbf{R} = \mathbf{U} \begin{bmatrix} \mathbf{H} \\ \\ \mathbf{O} \end{bmatrix} \mathbf{V}^T. \tag{B.2}$$

where $\mathbf{U}$ ($N_{reg} \times N_{reg}$) and $\mathbf{V}$ ($N_x \times N_x$) are orthogonal matrices, and $\mathbf{H}$ is a $N_x \times N_x$ diagonal matrix containing singular values. By changing variable

$$\mathbf{x}_1 = \mathbf{V}^T\mathbf{x}, \quad \mathbf{x} = \mathbf{V}\mathbf{x}_1, \tag{B.3}$$

Eq. (B.1) becomes

$$\begin{aligned} &||\mathbf{y} - \mathbf{C}\mathbf{V}\mathbf{x}_1||^2 + \alpha^2||\mathbf{U} \begin{bmatrix} \mathbf{H} \\ \\ \mathbf{O} \end{bmatrix} \mathbf{V}^T\mathbf{V}\mathbf{x}_1||^2 \\ =&||\mathbf{y} - \mathbf{C}\mathbf{V}\mathbf{x}_1||^2 + \alpha^2||\mathbf{H}\mathbf{x}_1||^2 = \text{mininum}, \end{aligned} \tag{B.4}$$

and the constraint becomes

$$\mathbf{V}\mathbf{x}_1 \geq \mathbf{0}. \tag{B.5}$$

Here if $N_{reg} < N_x$, zero rows are added to R so that $N_{reg} = N_x$.

Next, we change variable $\mathbf{x}_1$ by

$$\mathbf{x}_2 = \mathbf{H}\mathbf{x}_1, \quad \mathbf{x}_1 = \mathbf{H}^{-1}\mathbf{x}_2. \tag{B.6}$$

Eqs. (B.4) and (B.5) are then transformed to a standard ridge regression problem with linear inequality constraint

$$||\mathbf{y} - \mathbf{C}\mathbf{V}\mathbf{H}^{-1}\mathbf{x}_2||^2 + \alpha^2||\mathbf{x}_2||^2 = \text{minimum}, \tag{B.7}$$

$$\mathbf{V}\mathbf{H}^{-1}\mathbf{x}_2 \geq 0. \tag{B.8}$$

Then, we perform a second singular value decomposition

$$\mathbf{C}\mathbf{V}\mathbf{H}^{-1} = \mathbf{Q}\mathbf{S}\mathbf{W}^T, \tag{B.9}$$

and replace variable

$$\mathbf{x}_3 = \mathbf{W}^T\mathbf{x}_2, \quad \mathbf{x}_2 = \mathbf{W}\mathbf{x}_3. \tag{B.10}$$

Eqs. (B.7) and (B.8) then become

$$||\boldsymbol{\gamma} - \mathbf{S}\mathbf{x}_3||^2 + \alpha^2||\mathbf{x}_3||^2 = \text{minimum}, \tag{B.11}$$

$$\mathbf{V}\mathbf{H}^{-1}\mathbf{W}\mathbf{x}_3 \geq 0, \tag{B.12}$$

where the $N_x \times 1$ vector $\boldsymbol{\gamma}$ is defined by

$$\boldsymbol{\gamma} = \mathbf{Q}^T\mathbf{y} \tag{B.13}$$

Eq. (B.11) is identical to the following equation except for some constants independent of $\mathbf{x}_3$:

$$||\tilde{\boldsymbol{\gamma}} - \tilde{\mathbf{S}}\mathbf{x}_3||^2 = \text{minimum}, \tag{B.14}$$

where $N_x \times 1$ vector $\tilde{\boldsymbol{\gamma}}$ and $N_x \times N_x$ diagonal matrix $\tilde{\mathbf{S}}$ are defined by

$$\tilde{\gamma}_j = \gamma_j S_{jj}(S_{jj} + \alpha^2)^{-1/2}, \quad \tilde{S}_{jj} = (S_{jj} + \alpha^2)^{1/2}. \tag{B.15}$$

We obtain the final LDP problem by replacing variable

$$\mathbf{x}_4 = \tilde{\mathbf{S}}\mathbf{x}_3 - \tilde{\boldsymbol{\gamma}}, \quad \mathbf{x}_3 = \tilde{\mathbf{S}}^{-1}(\mathbf{x}_4 + \tilde{\boldsymbol{\gamma}}), \tag{B.16}$$

which transforms Eqs. (B.14) and (B.12) to

$$||\mathbf{x}_4||^2 = \text{minimum}, \tag{B.17}$$

$$\mathbf{V}\mathbf{H}^{-1}\mathbf{W}\tilde{\mathbf{S}}^{-1}\mathbf{x}_4 \geq -\mathbf{V}\mathbf{H}^{-1}\mathbf{W}\tilde{\mathbf{S}}^{-1}\tilde{\boldsymbol{\gamma}} \tag{B.18}$$

This LDP probelm is finally constructed and ready to be solved.

(2) *Solving LDP:* The problem represented by Eqs. (B.17) and (B.18) can be solved by a LDP algorithm developed by Lawson and Hanson (See Chap. 23 in Ref. [57]). Once the optimal solution $\mathbf{x}_4$ is obtained, the original solution is expressed as

$$\mathbf{x} = \mathbf{V}\mathbf{H}^{-1}\mathbf{W}\tilde{\mathbf{S}}^{-1}(\mathbf{x}_4 + \tilde{\boldsymbol{\gamma}}) \tag{B.19}$$

If the nonnegative constraint is not needed, one can simply set $\mathbf{x}_4 = \mathbf{0}$ in Eq (B.19).

References

[1] P. G. Debenedetti and F. H. Stillinger. Supercooled liquids and the glass transition. *Nature*, 410(6825):259–267, 2001.

[2] C. A. Angell. Formation of Glasses from Liquids and Biopolymers. *Science*, 267(5206):1924–1935, mar 1995.

[3] P. G. Debenedetti, T. M. Truskett, C. P. Lewis, and F. H. Stillinger. Theory of supercooled liquids and glasses: Energy landscape and statistical geometry perspectives. *Advances in Chemical Engineering*, 28:21–79, 2001.

[4] A. L. Greer. Metallic glasses. *Science (New York, N.Y.)*, 267(5206):1947–1953, 1995.

[5] W. H. Wang, C. Dong, and C. H. Shek. Bulk metallic glasses. *Materials Science and Engineering R: Reports*, 44(2-3):45–90, 2004.

[6] Y. Shirota. Photo- and electroactive amorphous molecular materials-molecular design, syntheses, reactions, properties, and applications. *J. Mater. Chem.*, 15:75–93, 2005.

[7] S. R. Forrest and M. E. Thompson. Introduction: Organic electronics and optoelectronics. *Chemical Reviews*, 107(4):923–925, 2007.

[8] J. M. V. Blanshard and P Lillford. *Glassy state in foods*. Nottingham University Press, 1993.

[9] J. H. Crowe, J. F. Carpenter, and L. M. Crowe. The role of vitrification in anhydrobiosis. *Annual review of physiology*, 60:73–103, 1998.

[10] L. Berthier. Dynamic Heterogeneity in Amorphous Materials. *Physics*, 4:42, May 2011.

[11] H. Sillescu. Heterogeneity at the glass transition: a review. *Journal of Non-Crystalline Solids*, 243(2-3):81–108, February 1999.

[12] M. D. Ediger. Spatially heterogeneous dynamics in supercooled liquids. *Annual review of physical chemistry*, pages 99–128, 2000.

[13] R. Richert. Heterogeneous dynamics in liquids: fluctuations in space and time, 2002.

[14] N. Lacevic, F. W. Starr, T. B. Schrø der, and S. C. Glotzer. Spatially heterogeneous dynamics investigated via a time-dependent four-point density correlation function. *The Journal of Chemical Physics*, 119(14):7372, 2003.

[15] A. Rahman. Correlations in the motion of atoms in liquid argon. *Phys. Rev.*, 136:A405–A411, Oct 1964.

[16] S. C. Glotzer, V. N. Novikov, and T. B. Schrø der. Time-dependent, four-point density correlation function description of dynamical heterogeneity and decoupling in supercooled liquids. *The Journal of Chemical Physics*, 112(2):509, 2000.

[17] G. Adam and J. H. Gibbs. On the Temperature Dependence of Cooperative Relaxation Properties in Glass-Forming Liquids. *The Journal of Chemical Physics*, 43(1):139, 1965.

[18] T. Geszti. Pre-vitrification by viscosity feedback. *Journal of Physics C: Solid State Physics*, 16(30):5805–5814, 1983.

[19] U. Bengtzelius, W. Götze, and A. Sjögren. Dynamics of supercooled liquids and the glass transition. *Journal of Physics C: Solid State Physics*, 17(33):5915–5934, 1984.

[20] W. Götze and L. Sjögren. Relaxation processes in supercooled liquids. *Reports on Progress in Physics*, 55(3):241–376, 1992.

[21] W. Götze and L. Sjögren. The mode coupling theory of structural relaxations. *Transport Theory and Statistical Physics*, 24(6-8):801–853, 1995.

[22] T. R. Kirkpatrick and D. Thirumalai. P-spin-interaction spin-glass models: Connections with the structural glass problem. *Physical Review B*, 36(10):5388–5397, 1987.

[23] T. R. Kirkpatrick. Dynamics of the Structural Glass Transition and the p-SpinInteraction Spin-Glass Model. *Physical Review Letters*, 58(20):2091–2094, 1987.

[24] T. R. Kirkpatrick, D. Thirumalai, and P. G. Wolynes. Scaling concepts for the dynamics of viscous liquids near an ideal glassy state. *Physical Review A*, 40(2):1045–1054, 1989.

[25] V. Lubchenko and P. G. Wolynes. Theory of structural glasses and supercooled liquids. *Annual review of physical chemistry*, 58:235–266, 2007.

[26] T. R. Kirkpatrick and D. Thirumalai. Colloquium: Random first order transition theory concepts in biology and physics. *Reviews of Modern Physics*, 87(1):183–209, March 2015.

[27] D. Chandler and J. P Garrahan. Dynamics on the way to forming glass: bubbles in space-time. *Annual review of physical chemistry*, 61:191–217, jan 2010.

[28] M. Goldstein. Viscous Liquids and the Glass Transition: A Potential Energy Barrier Picture. *The Journal of Chemical Physics*, 51(9):3728, 1969.

[29] F. H. Stillinger and T. A. Weber. Hidden structure in liquids. *Physical Review A*, 25(2):978–989, 1982.

[30] A. S. Argon and H. Y. Kuo. Free energy spectra for inelastic deformation of five metallic glass alloys. *Journal of Non-Crystalline Solids*, 37(2):241–266, apr 1980.

[31] A. N. Tsyplakov, Yu. P. Mitrofanov, A. S. Makarov, G. V. Afonin, and V. A. Khonik. Determination of the activation energy spectrum of structural relaxation in metallic glasses using calorimetric and shear modulus relaxation data. *Journal of Applied Physics*, 116(12):123507, sep 2014.

[32] W. Jiao, P. Wen, H. L. Peng, H. Y. Bai, B. A. Sun, and W. H. Wang. Evolution of structural and dynamic heterogeneities and activation energy distribution of deformation units in metallic glass. *Applied Physics Letters*, 102(10):101903, 2013.

[33] P. M. Chaikin and T. C. Lubensky. *Principles of condensed matter physics*, volume 1. Cambridge Univ Press, 2000.

[34] G. L. Squires. *Introduction to the theory of thermal neutron scattering*. Cambridge university press, 2012.

[35] L. Van Hove. Correlations in space and time and born approximation scattering in systems of interacting particles. *Physical Review*, 95(1):249–262, 1954.

[36] G. H. Vineyard. Scattering of slow neutrons by a liquid. *Physical Review*, 110(5):999–1010, 1958.

[37] V. Garcia Sakai. *Quasi-elastic neutron scattering.* Presentation in 13th Oxford School of Neutron Scattering, 2013.

[38] R. Salmon. Hamiltonian fluid mechanics. *Annual review of fluid mechanics*, 20(1):225–256, 1988.

[39] A. Gomberoff and S. A. Hojman. Non-standard Construction of Hamiltonian Structures. 5077:13, 1997.

[40] S. A. Hojman. The construction of a Poisson structure out of a symmetry and a conservation law of a dynamical system, 1999.

[41] D. Chandler. *Introduction to modern statistical mechanics.* Oxford University Press, 1987.

[42] J. C. Brown, P. N. Pusey, J. W. Goodwin, and R. H. Ottewill. Light scattering study of dynamic and time-averaged correlations in dispersions of charged particles. *Journal of Physics A: Mathematical and General*, 8(5):664, 1975.

[43] W. Hess and R. Klein. Dynamical properties of colloidal systems: 1. derivation of stochastic transport equations. *Physica A: Statistical Mechanics and its Applications*, 94(1):71–90, 1978.

[44] C. P. Lindsey and G. D. Patterson. Detailed comparison of the WilliamsWatts and ColeDavidson functions. *The Journal of Chemical Physics*, 73(7):3348, 1980.

[45] F. Alvarez, A. Alegra, and J. Colmenero. Relationship between the time-domain Kohlrausch-Williams-Watts and frequency-domain Havriliak-Negami relaxation functions. *Physical Review B*, 44(14), 1991.

[46] R. Zorn. Logarithmic moments of relaxation time distributions. *Journal of Chemical Physics*, 116(8):3204–3209, 2002.

[47] J. P. Hansen and I. R. McDonald. *Theory of simple liquids.* Elsevier, 1990.

[48] B. Davies and B. Martin. Numerical Inversion of the Laplace Transform: a Survey and Comparison of Methods. *Journal of Computational Physics*, 33:1–32, 1979.

[49] K. L. Kuhlman. Review of inverse Laplace transform algorithms for Laplace-space numerical approaches. *Numerical Algorithms*, 63(2):339–355, August 2012.

[50] J. Abate and W. Whitt. The Fourier-Series Methods for Inverting Transforms of Probability Distributions. *Queueing systems*, 10, n1-2:5–87, 1992.

[51] J. Abate and W. Whitt. A unified framework for numerically inverting laplace transforms. *INFORMS Journal on Computing*, 18(4):408–421, November 2006.

[52] A. M. Cohen. *Numerical Methods For Laplace Transform Inversion.* 2007.

[53] P. Valko and V. Vojta. *The List.* An bibliography of papers on numerical inversion of Laplace transform, 2001. `http://www.pe.tamu.edu/valko/public_html/Nil/LapLit.pdf`.

[54] H. Dubner and J. Abate. Numerical Inversion of Laplace Transforms by Relating Them to the Finite Fourier Cosine Transform. *Journal of the ACM*, 15(1):115–123, jan 1968.

[55] A. Talbot. The accurate numerical inversion of laplace transforms. *IMA Journal of Applied Mathematics (Institute of Mathematics and Its Applications)*, 23(1):97–120, 1979.

[56] J. Abate and P. P. Valkó. Multi-precision Laplace transform inversion. *International Journal for Numerical Methods in Engineering*, 60(5):979–993, 2004.

[57] C. L. Lawson and R. J. Hanson. *Solving least squares problems*, volume 161. SIAM, 1974.

[58] Michael Heath. *Scientific computing: an introductory survey.* The McGraw-Hill Companies Inc., New York, 2002.

[59] S. W. Provencher. A constrained regularization method for inverting data represented by linear algebraic or integral equations. *Computer Physics Communications*, 27(3):213–227, sep 1982.

[60] A. N. Tikhonov and V. Y. Arsenin. *Solutions of ill-posed problems*. WH Winston, Washington, DC, 1977.

[61] R. Tibshirani. Regression shrinkage and selection via the lasso. *Journal of the Royal Statistical Society. Series B (Methodological)*, pages 267–288, 1996.

[62] B. Efron and T. Hastie. Least angle regression. *The Annals of ...*, 32(2):407–499, 2004.

[63] H. Zou and T. Hastie. Regularization and variable selection via the elastic net. *Journal of the Royal Statistical Society: Series B (Statistical Methodology)*, 67(2):301–320, April 2005.

[64] S. Pressé, K. Ghosh, J. Lee, and K. A. Dill. Principles of maximum entropy and maximum caliber in statistical physics. *Reviews of Modern Physics*, 85(3):1115–1141, 2013.

[65] N. Wu. *The maximum entropy method*, volume 32. Springer Science & Business Media, 2012.

[66] S Fi Burch, SF Gull, and John Skilling. Image restoration by a powerful maximum entropy method. *Computer Vision, Graphics, and Image Processing*, 23(2):113–128, 1983.

[67] S. F. Gull and J. Skilling. Maximum entropy method in image processing. *IEE Proceedings F Communications, Radar and Signal Processing*, 131(6):646–659, 1984.

[68] A. L. Berger, V. J. D. Pietra, and S. A. D. Pietra. A maximum entropy approach to natural language processing. *Comput. Linguist.*, 22(1):39–71, March 1996.

[69] A. K. Livesey and J. C. Brochon. Analyzing the distribution of decay constants in pulse-fluorimetry using the maximum entropy method. *Biophysical journal*, 52(5):693–706, 1987.

[70] M. Sakata and M. Sato. Accurate structure analysis by the maximum-entropy method. *Acta Crystallographica Section A*, 46(4):263–270, Apr 1990.

[71] R. N. Silver, D. S. Sivia, and J. E. Gubernatis. Maximum-entropy method for analytic continuation of quantum Monte Carlo data. *Physical Review B*, 41(4):2380–2389, 1990.

[72] J. C. Brochon. Maximum entropy method of data analysis in time-resolved spectroscopy. *Methods in Enzymology*, 240(1987):262–311, 1994.

[73] V. A. Morozov. *Methods for solving incorrectly posed problems*. Springer Science & Business Media, 2012.

[74] G. H. Golub, M. Heath, and G. Wahba. Generalized cross-validation as a method for choosing a good ridge parameter. *Technometrics*, 21(2):215–223, 1979.

[75] P. C. Hansen. Analysis of Discrete Ill-Posed Problems by Means of the L-Curve. *SIAM Review*, 34(4):561–580, Dec 1992.

[76] P. C. Hansen and D. P. OLeary. The Use of the L-Curve in the Regularization of Discrete Ill-Posed Problems. *SIAM Journal on Scientific Computing*, 14(6):1487–1503, nov 1993.

[77] S. W. Provencher. Contin: A general purpose constrainded regularization program for inverting noisy linear algebraic and integral equations. *Computer Physics Communications*, 35(3):C–818–C–819, September 1984.

[78] P. E. Gill, W. Murray, and M. H. Wright. *Practical optimization*. London: Academic Press, 1981.

[79] N. Gould and P. L. Toint. Preprocessing for quadratic programming. *Mathematical Programming*, 100(1):95–132, 2004.

[80] A. A. Istratov and O. F. Vyvenko. Exponential analysis in physical phenomena. *Review of Scientific Instruments*, 70(2):1233–1257, 1999.

[81] R. Kohlrausch. Theorie des elektrischen rckstandes in der leidener flasche. *Ann. Phys. Chem. (Leipzig)*, 91:179–214, 1874.

[82] G. Williams and D. C. Watts. Non-symmetrical dielectric relaxation behaviour arising from a simple empirical decay function, 1970.

[83] P. Humbert. Nouvelles Correspondances Symboliques. *Bulletin des Sciences Mathématiques. Deuxième Série*, 69:121–129, 1945.

[84] H. Pollard. The representation of $e^{-x^{\lambda}}$ as a laplace integral. *Bull. Amer. Math. Soc.*, 52(10):908–910, 10 1946.

[85] M. N. Berberan-Santos. Analytical inversion of the Laplace transform without contour integration: Application to luminescence decay laws and other relaxation functions. *Journal of Mathematical Chemistry*, 38(2):165–173, August 2005.

[86] M. N. Berberan-Santos, E. N. Bodunov, and B. Valeur. Mathematical functions for the analysis of luminescence decays with underlying distributions 1. Kohlrausch decay function (stretched exponential). *Chemical Physics*, 315(1):171–182, 2005.

[87] W. Kob and H. C. Andersen. Testing mode-coupling theory for a supercooled binary Lennard-Jones mixture I: The van Hove correlation function. *Physical Review E*, 51(5), 1995.

[88] W. Kob and H. C. Andersen. Testing mode-coupling theory for a supercooled binary Lennard-Jones mixture. II. Intermediate scattering function and dynamic susceptibility. *Physical Review E*, 52(4), 1995.

[89] Y. Jung, J. P. Garrahan, and D. Chandler. Excitation lines and the breakdown of Stokes-Einstein relations in supercooled liquids. *Physical Review E*, 69(6):061205, Jun 2004.